MATERIALS SCIENCE

Robust, high-performance n-type organic semiconductors

Toshihiro Okamoto[1,2,3]*†, Shohei Kumagai[1†], Eiji Fukuzaki[4], Hiroyuki Ishii[5], Go Watanabe[6], Naoyuki Niitsu[1], Tatsuro Annaka[1], Masakazu Yamagishi[7], Yukio Tani[4], Hiroki Sugiura[4], Tetsuya Watanabe[4], Shun Watanabe[1,2,3], Jun Takeya[1,2,8]

Organic semiconductors (OSCs) are important active materials for the fabrication of next-generation organic-based electronics. However, the development of n-type OSCs lags behind that of p-type OSCs in terms of charge-carrier mobility and environmental stability. This is due to the absence of molecular designs that satisfy the requirements. The present study describes the design and synthesis of n-type OSCs based on challenging molecular features involving a π-electron core containing electronegative N atoms and substituents. The unique π-electron system simultaneously reinforces both electronic and structural interactions. The current n-type OSCs exhibit high electron mobilities with high reliability, atmospheric stability, and robustness against environmental and heat stresses and are superior to other existing n-type OSCs. This molecular design represents a rational strategy for the development of high-end organic-based electronics.

INTRODUCTION

The aggregation of π-electron systems in organic semiconductors (OSCs) via weak intermolecular interactions can produce soft, lightweight, and mechanically flexible materials. These properties are in contrast to those of covalently bonded inorganic semiconductors such as silicon. The intrinsic high solubility of OSCs in organic solvents also enables low-cost mass production using solution-processing techniques (*1*–*4*). Charge-carrier mobility (referred to as mobility) is one of the most important performance indicators for a semiconductor. For weakly bound OSCs, mobility is determined primarily by effective mass (m^*) that results from the overlap of molecular orbitals between two adjacent molecules [transfer integral (t)] (*5*–*7*). However, reductions in dynamic disorder originating from thermally induced intermolecular vibrations (that is, molecular motion) (*8*–*14*) also can be important factors for improving mobility. Recent advances in the design of p-type, bent-shaped π-electron systems (*15*–*21*) have resulted in two-dimensional (2D) charge-transport herringbone-type packing structures due to multiple intermolecular interactions as well as suppressed molecular motions (Fig. 1A). These materials have been incorporated into solution-processed transistors and have exhibited hole mobilities exceeding 10 $\mathrm{cm^2\ V^{-1}\ s^{-1}}$ and ambient stability and thermal durability features that are required for practical applications in future high-end printed electronics (*15*, *16*, *20*, *22*). The n-type OSCs have been developed on the basis of electron-deficient π-cores (*23*–*25*), such as arylene diimide derivatives (*26*), and hence, some high electron mobilities greater than 5 $\mathrm{cm^2\ V^{-1}\ s^{-1}}$ have been reported (*27*–*29*). However, n-type OSCs showing the same level of performance have not yet been achieved because of the lack of molecular design strategies based on suppression of molecular motions.

Ideally, a high-performance n-type OSC would have features such as a planar, rigid molecular structure over the entire extended π-electron framework, which promotes carrier transport via intermolecular π-π overlap in the solid state. In addition, the lowest unoccupied molecular orbitals (LUMOs) engaged in the electron transport process must have energy levels (E_{LUMO}) lower than −4.0 eV to protect the material against oxidation by ambient O_2 and H_2O (*25*). These properties would allow solution processing under ambient air, which would lower the cost of manufacturing practical electronic devices such as logic circuits. Last, the molecular motion of n-type OSCs also should be suppressed to achieve consistent and effective orbital overlaps.

Because of the unique electronic requirements for n-type OSCs ($E_{\mathrm{LUMO}} < -4.0$ eV), a common molecular design strategy involves the introduction of strong electron-withdrawing groups such as imide, cyano, and halogen moieties (*25*). In particular, PDI–FCN$_2$ (*30*), in which the perylene π-core contains one cyano group on each side at the bay positions and linear fluoroalkyl substituents on the imide N, exhibits high electron mobilities exceeding 1 $\mathrm{cm^2\ V^{-1}\ s^{-1}}$ in solution-grown single-crystalline (SC) transistors under ambient conditions (*27*, *31*, *32*). This compound also shows free-electron–like carrier behaviors, such as band-like transport (*27*). However, simultaneously obtaining effective orbital overlap and suppression on molecular motions using this strategy is difficult. Because almost all n-type OSCs reported, including PDI–FCN$_2$, form 2D brickwork-type packing structures, these compounds exhibit less effective orbital overlaps with a higher degree of anisotropy. In particular, the overlap is reduced obviously in the lateral direction of the molecule (Fig. 1B) compared with that in high-mobility p-type OSCs having herringbone-type packing structures (Fig. 1A). This limited overlap leads to poor charge transport in n-type OSCs. This difficulty in achieving intermolecular interactions in the aggregated form of the material has impeded the development of high-performance n-type OSCs with

---

[1]Material Innovation Research Center (MIRC) and Department of Advanced Materials Science, Graduate School of Frontier Sciences, The University of Tokyo, 5-1-5 Kashiwanoha, Kashiwa, Chiba 277-8561, Japan. [2]National Institute of Advanced Industrial Science and Technology (AIST)–University of Tokyo Advanced Operando-Measurement Technology Open Innovation Laboratory (OPERANDO-OIL), AIST, 5-1-5 Kashiwanoha, Kashiwa, Chiba 277-8561, Japan. [3]PRESTO, JST, 4-1-8 Honcho, Kawaguchi, Saitama 332-0012, Japan. [4]Fujifilm Corp., 577 Ushijima, Kaisei-machi, Ashigarakami-gun, Kanagawa 258-8577, Japan. [5]Department of Applied Physics, Faculty of Pure and Applied Sciences, University of Tsukuba, 1-1-1 Tennodai, Tsukuba, Ibaraki 305-8573, Japan. [6]Department of Physics, School of Science, Kitasato University, 1-15-1 Kitasato, Minami-ku, Sagamihara, Kanagawa 252-0373, Japan. [7]Department of Applied Chemistry and Chemical Engineering, National Institute of Technology, Toyama College, 13 Hongo-machi, Toyama City, Toyama 939-8630, Japan. [8]MANA, National Institute for Materials Science (NIMS), 1-1 Namiki, Tsukuba 205-0044, Japan.
*Corresponding author. Email: tokamoto@k.u-tokyo.ac.jp
†These authors contributed equally to this work.

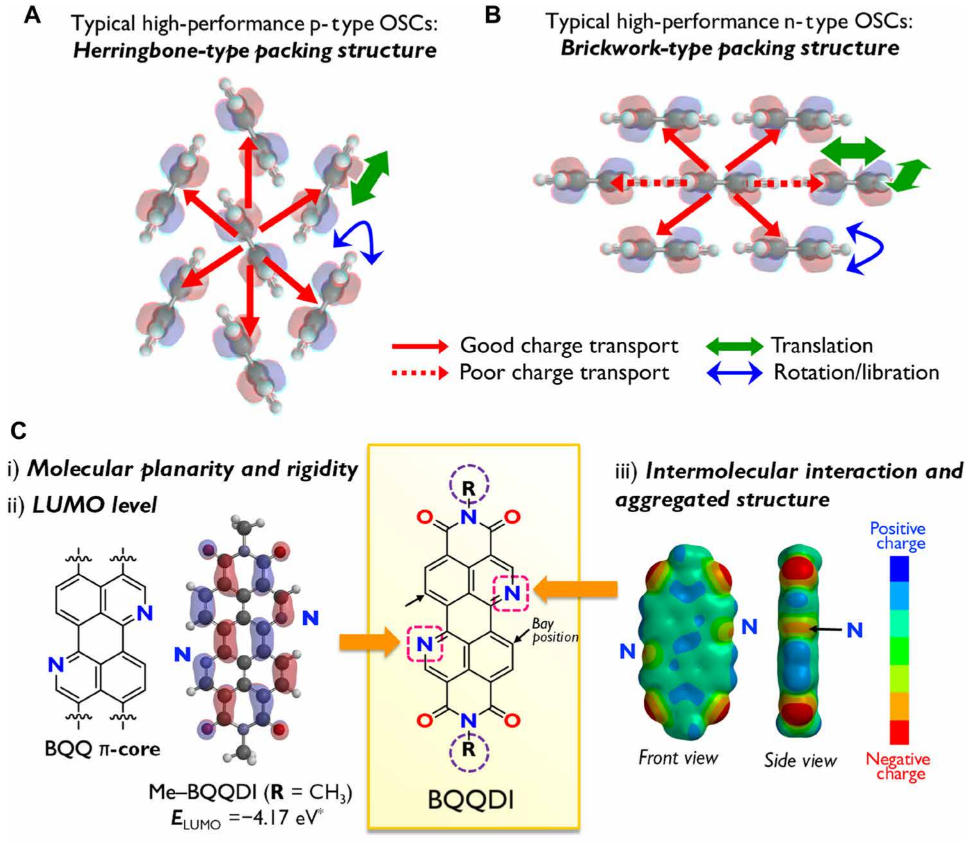

* Calculated at the B3LYP/6-31+G(d)//6-31G(d) level

Fig. 1. Typical aggregated structures of high-performance OSCs and the molecular design of BQQDI. (**A** and **B**) Typical herringbone- and brickwork-type packing structures of high-performance p-type and n-type OSCs. (**C**) Chemical structures and molecular designs used in this work. Displayed molecular orbital is the LUMO. Right side shows the calculated electrostatic potential map.

limited molecular motions together with suitable robustness for use in high-end devices.

The present report proposes a strategy for the molecular design of n-type OSCs, based on the concept of a π-core containing electronegative N atoms, where the N atoms play multiple roles for tuning and enhancing electronic and structural properties. The base compound used in this work, 3,4,9,10-benzo[*de*]isoquinolino[1,8-*gh*]quinolinetetracarboxylic diimide (BQQDI) (Fig. 1C), exhibits several beneficial features, including a rigid, planar structure based on the BQQ π-core that allows effective charge transport. In addition, BQQDI has a molecular structure and orbital configuration similar to those of perylene diimide (PDI), which has been widely studied. However, the replacement of two bay C sites with N atoms should theoretically lower the LUMO level from −3.81 eV in the case of methyl-substituted PDI (Me–PDI) to −4.17 eV for Me–BQQDI, thus improving the chemical stability of n-type transistors made from this compound (*25*). Last, the presence of electronegative N atoms in BQQDI allows alternating electronegative/electropositive positions, corresponding to O and N and C-H moieties, respectively, along the lateral direction of the molecule, which is expected to promote core-to-core interactions, improving intermolecular charge transport and increasing both chemical and physical robustness. In addition, the alternating electronegative/electropositive feature should play a key role to order BQQDI π-cores in the solids. This is in contrast to a previous work based on the synthesis of acenes containing N intended solely to reduce LUMO levels (*33*). In particular, in the current strategy, the goal was brickwork-type packing structures with strong core-to-core interactions due to the designed contrast of electronegativity for high-performance n-type OSCs. Substituents can be added readily to the imide units in this new compound as a means of fine-tuning the molecular ordering.

In the present study, the linear alkyl- and phenylalkyl-substituted BQQDIs (C_8–BQQDI and PhC_2–BQQDI, respectively) were synthesized and assessed. Both of these compounds were obtained from the key precursor 3,4,9,10-benzo[*de*]isoquinolino[1,8-*gh*]quinolinetetracarboxylic dianhydride (BQQ–TCDA) (Fig. 2A). These BQQDI derivatives exhibit substantial chemical and thermal stability during repeated recrystallization and sublimation. The LUMO levels of BQQDIs were estimated to be −4.11 eV, indicating that alkyl-substituted BQQDI analogs could potentially be processed into devices that are durable under ambient conditions. In the aggregated structures, the BQQDI units undergo desired lateral hydrogen-bonding interactions between N, H, and O within the 2D brickwork-type packing structure, indicating effective orbital overlap in the lateral direction. PhC_2–BQQDI aggregates through the terminal phenyl groups of the phenethyl units via C—H···π intermolecular and interlayer interactions. This feature results in a 2D brickwork-type packing structure that promotes charge transport as well as a highly stable crystal phase. The PhC_2–BQQDI exhibits impressive semiconductor performance, with electron mobility values up to 3.0 $cm^2\ V^{-1}\ s^{-1}$, with high reliability in a solution-crystallized thin-film transistor (TFT).

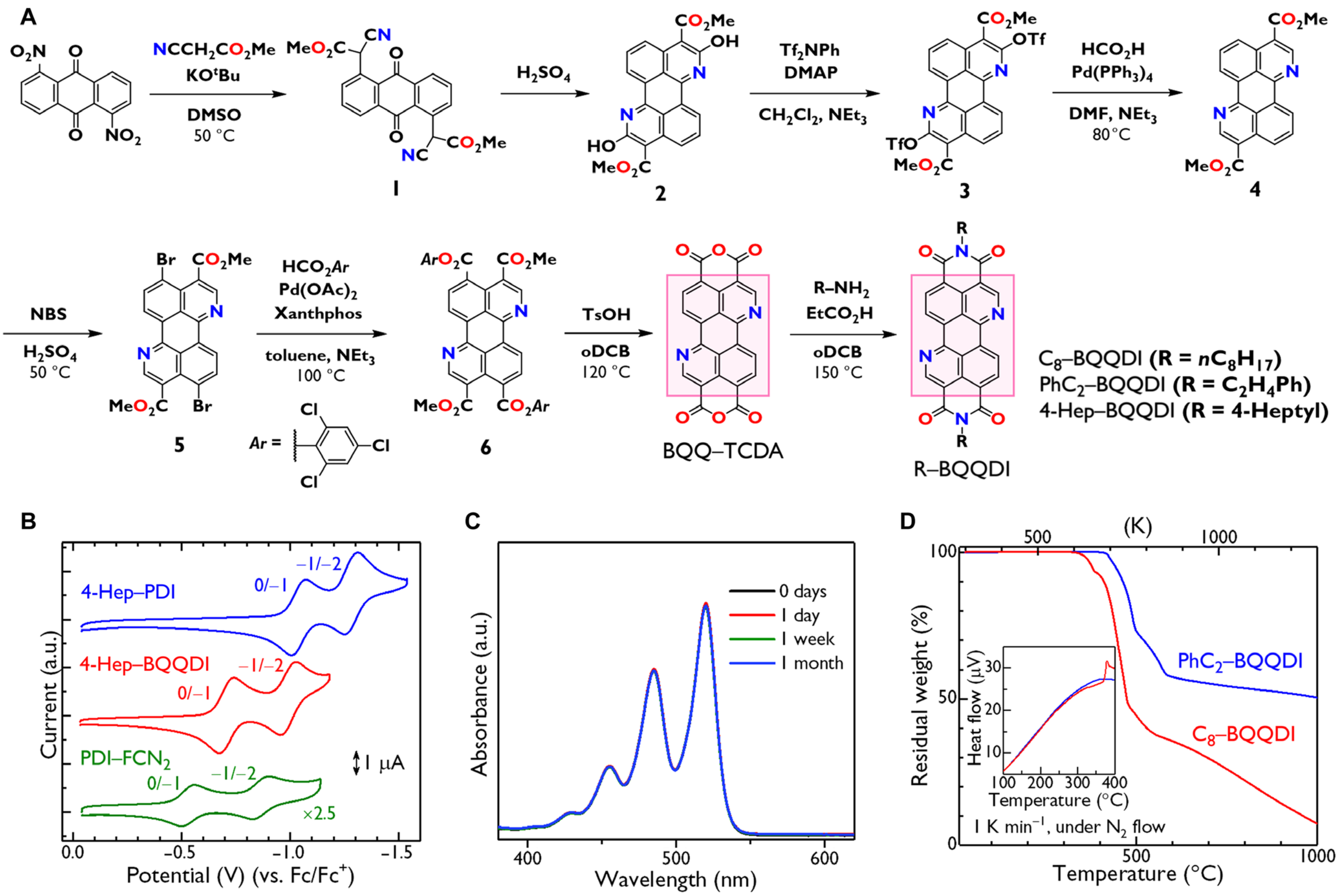

Fig. 2. Synthesis and fundamental chemical properties of BQQDI derivatives. (**A**) Scheme for the syntheses of BQQ–TCDA and BQQDI derivatives (C$_8$–BQQDI, PhC$_2$–BQQDI, and 4-Hep–BQQDI). (**B**) Cyclic voltammograms obtained from 4-Hep–PDI (0.5 mM; blue), 4-Hep–BQQDI (0.5 mM; red), and PDI–FCN$_2$ (0.2 mM; green) in benzonitrile. (**C**) Time-dependent UV-vis spectra obtained from 4-Hep–BQQDI in benzonitrile (4×10^{-6} M) under ambient air. (**D**) TG plots obtained from PhC$_2$–BQQDI (blue) and C$_8$–BQQDI (red) at a heating rate of 1 K min^{-1} under a stream of nitrogen. Inset: DTA data up to 400°C. a.u., arbitrary units.

This value is twice that of PDI–FCN$_2$ processed into the same type of device using the same technique. The PhC$_2$–BQQDI also demonstrates band-like electron transport behavior. Band calculations and basic theoretical considerations indicate that, although the m^* value of PhC$_2$–BQQDI is substantially larger than that of PDI–FCN$_2$, the former exhibits higher electron mobility. This can be explained by assessing the dynamic fluctuations of transfer integrals induced by molecular motions. These analyses show that charge transport may proceed more efficiently in PhC$_2$–BQQDI. Last, PhC$_2$–BQQDI–based transistors exhibit durability during air and thermal stress tests up to at least 150°C. PhC$_2$–BQQDI is able to withstand photolithography processes for the fabrication of organic complementary metal-oxide semiconductor (CMOS) devices. The current study demonstrates the viability of fabricating chemically and physically robust devices as a result of applying this new molecular design concept based on a combination of π-core and substituent engineering.

RESULTS AND DISCUSSION

Synthesis and fundamental properties

Extensive effort was applied to determining a viable synthetic route to the preparation of the new compound BQQ–TCDA as a key precursor for BQQDI derivatives, due to the poor selectivity and low reactivity of the N-containing π-core as illustrated in Fig. 2A. Compounds **1** and **2** were prepared according to a previously reported procedure using 1,5-dinitroanthraquinone as a starting material (*34*, *35*). After synthesis of triflates **3**, reduction using formic acid, base, and Pd(0) yielded compound **4** in high yield. Dibromination and then palladium-catalyzed carbonylation using 2,4,6-trichlorophenyl formate (*36*) gave aryl ester **6**, which was lastly converted to BQQ-TCDA. Subsequently, the reactions of BQQ–TCDA with octylamine and phenethylamine gave the desired BQQDI derivatives C$_8$–BQQDI and PhC$_2$–BQQDI in high yields. A BQQDI analog substituted with a branched alkyl group (4-Hep–BQQDI) also was prepared to allow evaluation of the fundamental properties of alkyl-substituted BQQDIs. The LUMO levels of 4-Hep–BQQDI and of its PDI counterpart (4-Hep–PDI) were estimated to be −4.11 and – 3.78 eV, respectively, on the basis of the first half-reduction potentials obtained from cyclic voltammograms, while PDI–FCN$_2$ showed a much deeper LUMO level of −4.28 eV under the same conditions (Fig. 2B and table S3). The electrochemical LUMO levels of the alkyl-substituted BQQDIs are consistent with theoretical calculations that predict values substantially below −4.0 eV, indicating that alkyl-substituted BQQDI analogs could potentially be processed into devices that show durability under ambient conditions (*25*). The ultraviolet-visible (UV-vis) absorption spectra acquired from 4-Hep–BQQDI demonstrate negligible changes over the span of at least 1 month, indicating exceptional chemical stability under ambient conditions (Fig. 2C).

The thermal stabilities of C_8–BQQDI and PhC_2–BQQDI and of their PDI counterparts (C_8–PDI, PhC_2–PDI, and PDI–FCN_2), as well as the possibility of purification by sublimation and crystal-phase transition temperatures, were evaluated by thermogravimetry–differential thermal analysis (TG–DTA) under a nitrogen gas flow (Fig. 2D and fig. S18). The TG analyses demonstrated that the temperatures associated with 5% mass loss ($T^{95\%}$) were 377, 421, 402, and 429°C for C_8–BQQDI, PhC_2–BQQDI, C_8–PDI, and PhC_2–PDI, respectively. These values are all sufficiently high to withstand external heat stresses. Note that the DTA data showed no obvious phase transitions from the initial crystal phase for C_8–BQQDI and PhC_2–BQQDI (Fig. 2D, inset). The excellent thermal stability and highly stable crystal phases of these BQQDI variants would ensure consistent crystalline structures throughout various device fabrication processes as well as during operations at high temperatures.

Molecular and packing structures and theoretical calculations

The molecular and packing structures of these compounds were determined to verify the molecular designs and to investigate charge transport capabilities. These investigations were performed using single-crystal x-ray diffraction to assess C_8–BQQDI and PhC_2–BQQDI and their PDI counterparts at room temperature. The molecular and packing structures of the BQQDI compounds, PDI–FCN_2 and other PDI derivatives are provided in Figs. 3 and 4, where results of the PDI counterparts are provided as references. The BQQ cores of these molecules all exhibit planar conformations. As expected, the intermolecular interactions involve predominantly two types of attractive lateral interactions, based on close-contact C—H···O groups ($d_{\mathrm{H\cdots O}}$: 2.516 and 2.497 Å) and C—H···N groups ($d_{\mathrm{N\cdots H}}$: 2.488 and 2.412 Å) to form four-site hydrogen bonding (*37*). Short π-stacking distances (d_π: 3.247 and 3.249 Å) were observed for C_8–BQQDI and PhC_2–BQQDI, such that these compounds adopt 2D brickwork-type packing structures in the *ab*-plane. Owing to edge-to-face C—H···π interactions between the terminal phenyl groups of phenethyl units, PhC_2–BQQDI exhibits a more highly ordered packing structure in the *ab*-plane (Fig. 3B). The C_8–PDI and PhC_2–PDI formed 1D-like π-stacking structures with d_π = 3.337 and 3.491 Å and only two short hydrogen-bonding interactions between an O atom of the imide group and a terminal H atom of the perylene moiety ($d_{\mathrm{H\cdots O}}$: 2.494 and 2.417 Å) (Fig. 4, A and B). These molecular arrangements with larger displacements along the molecular longitudinal direction compared with those in BQQDIs resulted from the relatively weak core-to-core interactions between perylene groups, which induced an obvious degree of anisotropy and poor charge-transport characteristics along the lateral direction (Fig. 4, C to E).

To further investigate these effects, we calculated the interaction energy between adjacent molecules in the lateral direction (tables S1 and S2), and an absolute value of 7.97 kcal mol^{-1} (0.346 eV) was found from the crystal structure of C_8–BQQDI with its side chains substituted with hydrogen. The interactions for the BQQDI systems were stronger than those for the PDI-based compounds [5.40 kcal mol^{-1} (0.234 eV) based on the crystal structure of C_8–PDI with its side chains substituted with hydrogen]. Within BQQDI analogs, the interaction energy for PhC_2–BQQDI [8.48 kcal mol^{-1} (0.368 eV)] was slightly larger than that for C_8–BQQDI [7.79 kcal mol^{-1} (0.338 eV)] because of the additional force imparted by the presence of the PhC_2 substituent. In contrast to the other PDI compounds, PDI–FCN_2 (which contains cyano groups at two bay positions on the π-core) formed a 2D brickwork-type packing structure based on two sites associated with weak C≡N···H short contacts ($d_{\mathrm{N\cdots H}}$: 2.441 Å). The absolute intermolecular interaction energy for PDI–FCN_2 [3.37 kcal mol^{-1} (0.146 eV)] also was lower than that for the PDI-based compounds. From these results, PhC_2–BQQDI would be expected to have the most effective charge transport in the lateral direction, as well as superior suppression of molecular motions and a highly stabilized crystal phase.

On the basis of the packing structures of the BQQDI and PDI analogs, the transfer integral (*t*) values were calculated to investigate the potential applications of these compounds as n-type OSCs (*6*). The PhC_2–BQQDI had large positive *t* values of +91 meV (t_1) and + 59 meV (t_2) in the π-stacking directions (which exceeded those of C_8–BQQDI) and an unexpectedly large *t* value of +19 meV (t_3) in the lateral direction (Fig. 3, D and E). The PDI–FCN_2 had large positive t_1 and negative t_2 values along with a small negative t_3, indicating less balanced intermolecular overlaps (Fig. 3F). The results for C_8–PDI and PhC_2–PDI were similar to those for PDI–FCN_2 (Fig. 4, C and D).

Initial transistor evaluations based on PC films

The initial evaluations of these n-type OSCs in terms of electron mobility (μ_e), threshold voltage (V_{th}), and stability under ambient conditions in transistors were performed by preparing polycrystalline TFTs (PC-TFTs) via vacuum evaporation. These devices were fabricated with BQQDI analogs, and the performance of their PDI counterparts were studied under both inert and ambient atmospheres (Fig. 5, A to D; fig. S20, A to F; and table S5). These PC-TFTs were first evaluated in an Ar-filled glovebox, and all materials exhibited moderate n-type transistor performances. The TFTs incorporating the two BQQDI derivatives exhibited small V_{th} values and negligible hysteresis during gate-voltage (V_G) sweeps under both inert and ambient conditions, while PDI compounds (with the exception of PDI–FCN_2) showed drastic degradation of TFT performance, especially V_{th}, and exhibited clockwise hysteresis after exposure to ambient air. This device instability in response to air exposure is attributed to the shallow E_{LUMO} of C_8–PDI and PhC_2–PDI (> −4.0 eV). Thus, shelf-life testing under ambient air was performed using PC-TFTs made with the BQQDI-based compounds and PDI–FCN_2 over approximately 1 month (fig. S20, G to K). The PC-TFTs made with the BQQDI analogs showed slight decreases in μ_e and negative V_{th} shifts throughout these trials, while the PDI–FCN_2 device also underwent a slight decrease in μ_e but exhibited a larger and positive V_{th} shift. These results confirm the superior, prolonged stability of BQQDI materials under ambient air compared to that of PDI–FCN_2, likely due to the robust aggregated morphologies resulting from their crystal structures (*38*). Therefore, the BQQDI analogs were confirmed to be the most air-stable n-type OSCs among those examined.

Transistor evaluations based on SC films

The air-stable n-type OSC candidates C_8–BQQDI, PhC_2–BQQDI, and PDI–FCN_2 were investigated further as SC-TFTs to clarify their intrinsic electron-transporting capabilities in the absence of grain boundaries (*39*). The SC thin films were grown successfully using the

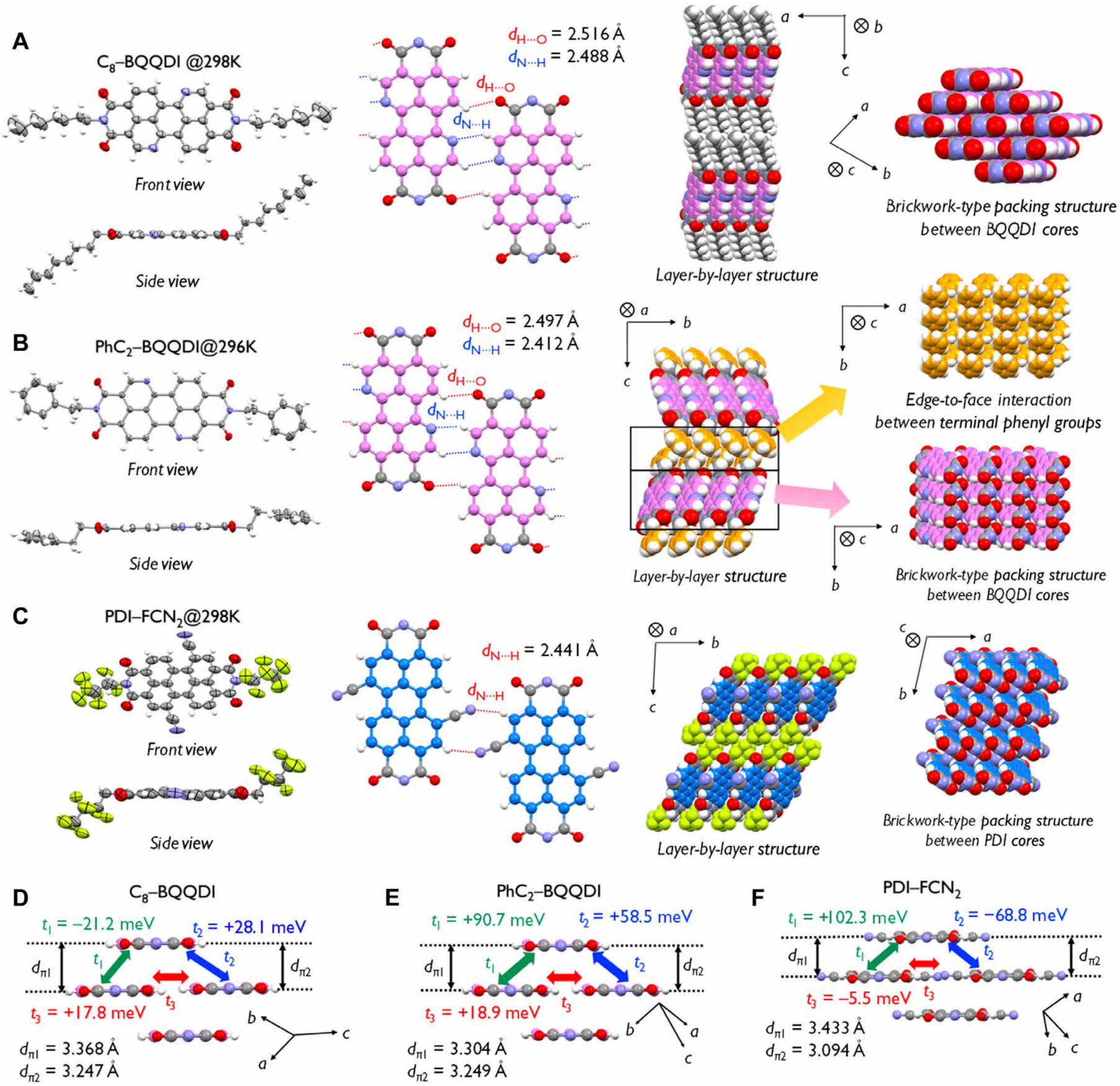

Fig. 3. Crystal structures and results of electron transport calculations for BQQDIs and PDI–FCN$_2$. (**A** to **F**) Aggregate structures in single crystals and results of charge transport calculations based on structural coordination. For C$_8$–BQQDI: (A) lateral intermolecular interactions and short contacts, (D) short contacts and estimates of transfer integrals in the direction of brickwork-type packing. For PhC$_2$–BQQDI: (B) lateral intermolecular interactions and short contacts, (E) short contacts and estimation of transfer integrals in the direction of brickwork-type packing. For PDI–FCN$_2$: (C) lateral intermolecular interactions and short contacts, (F) short contacts and estimates of transfer integrals in the direction of brickwork-type packing.

edge-casting method, a sophisticated technique (*40*). The SC-TFT characteristics of representative devices are shown in Fig. 5 (E to G) for the device made with PhC$_2$–BQQDI and in fig. S23 for the units incorporating C$_8$–BQQDI and PDI–FCN$_2$. These units exhibit typical n-channel outputs and transfer characteristics. The typical μ_e value for PhC$_2$–BQQDI device was estimated to be 3.0 cm^2 V^{-1} s^{-1} with a reliability factor of 89% (*41*), which was twice as high as that obtained using PDI–FCN$_2$ (1.3 cm^2 V^{-1} s^{-1}) (*31*) and an order of magnitude greater than that for the C$_8$–BQQDI device (0.33 cm^2 V^{-1} s^{-1}) in the saturation regime under the same conditions. Furthermore, gated Hall-effect measurements, which can be used to assess the degree of charge delocalization in OSC solids, confirmed bank-like electron transport in the case of the high-performance PhC$_2$–BQQDI device (Fig. 5H and fig. S26), which showed the same behavior as the PDI–FCN$_2$ unit. The estimated Hall mobility (μ_{Hall}) of 4.08 cm^2 V^{-1} s^{-1} for the PhC$_2$–BQQDI device verified the intrinsic high electron-transporting capability of this material (*41*).

Understanding carrier-transporting capability

To further understand the carrier-transporting capability of these materials in the bulk state based on band theory, LUMO band structures of the experimental crystal structures were also calculated, using the tight-binding approximation with the periodic boundary condition. In the band transport, the electron mobility is inversely proportional to m^*, as in the equation $\mu = q\tau/m^*$ (μ, mobility; q, elementary charge; τ, relaxation time; m^*, effective mass) (*42*). The m^* values for the BQQDI analogs and for PDI–FCN$_2$ were estimated from the band dispersion at the base of their LUMO bands, and the smallest

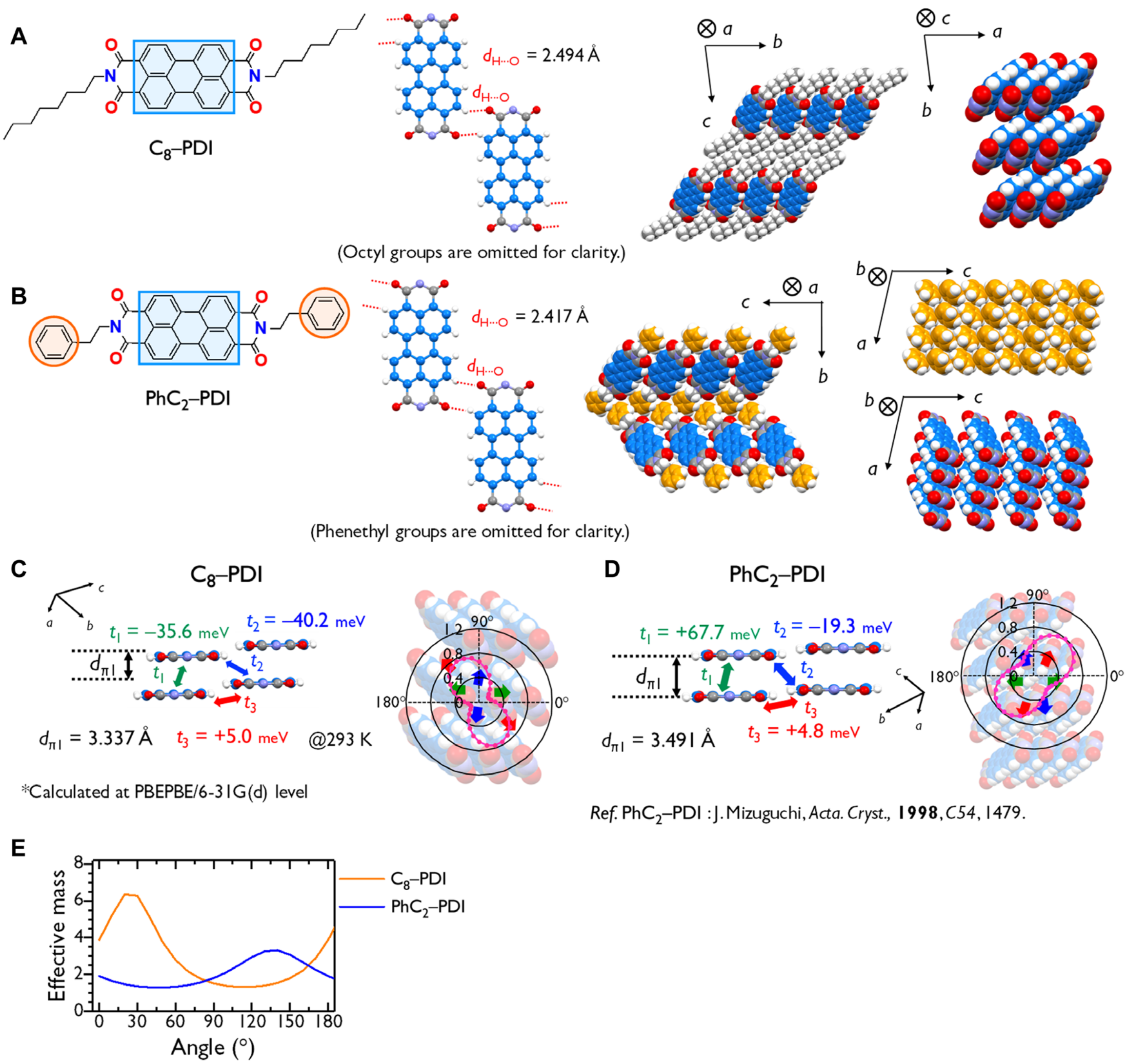

Ref. PhC$_2$–PDI : J. Mizuguchi, *Acta. Cryst.*, **1998**, *C54*, 1479.

Fig. 4. Packing structures and electron transport properties calculated for C$_8$–PDI and PhC$_2$–PDI. Molecular and crystal structures of (**A**) C$_8$–PDI and (**B**) PhC$_2$–PDI PhC2–PDI. Transfer integrals and angle-resolved values of the inverse of effective mass for (**C**) C$_8$–PDI and (**D**) PhC$_2$–PDI. (**E**) Angle-resolved effective mass. The effective mass is shown in unit of the rest mass of an electron.

angle-resolved effective masses for these compounds were similar, ranging from 0.83 to 1.34 (The effective mass is shown in unit of the rest mass of an electron.). The inverse of the angle-resolved effective mass ($1/m^*$) associated with PhC$_2$–BQQDI and PDI–FCN$_2$ conducting layers had a more elliptical contour than that of C$_8$–BQQDI (Fig. 5, I to L). The m^* values for PDI–FCN$_2$ also were much smaller than those of PhC$_2$–BQQDI, suggesting that the former is the best n-type OSC among the various derivatives. The PhC$_2$–BQQDI also was more isotropic and had greater charge transport capability than C$_8$–BQQDI. The SC-TFT data indicated that the higher μ_e obtained when using PhC$_2$–BQQDI compared to that obtained with PDI–FCN$_2$ cannot be explained solely on the basis of their respective effective masses. Judging from their band-like transport nature, the difference in performance between PhC$_2$–BQQDI and PDI–FCN$_2$ can be ascribed not only to variations in m^* but also to those in τ. According to band theory, μ is proportional to both $1/m^*$ and τ; hence, a longer τ arising from suppressed molecular motions can compensate for a smaller value of $1/m^*$ (*43*). Molecular dynamics (MD) simulations demonstrated reduced molecular motion in the case of PhC$_2$–BQQDI compared to PDI–FCN$_2$, and assessments of dynamic fluctuations of transfer integrals of these compounds confirmed that the variation in t_1, which was estimated from the SD (σ) in the histogram, was much smaller in PhC$_2$–BQQDI than in PDI–FCN$_2$ (Fig. 5, M to O and figs. S28 to S30). Therefore, molecular motions were suppressed successfully for PhC$_2$–BQQDI, such that an increase in τ could be derived. This effect is due to the combination of the BQQDI π-core and the use of PhC$_2$ substituents.

Device durability and applications

The durability of PhC$_2$–BQQDI SC-TFT in response to atmospheric and thermal stresses was examined. During atmospheric stability trials, no notable decreases in μ_e and V_{th} were detected over the span of half a year (Fig. 6, A and B). The initial deterioration observed may have been caused by evaporation of residual solvent in the crystal

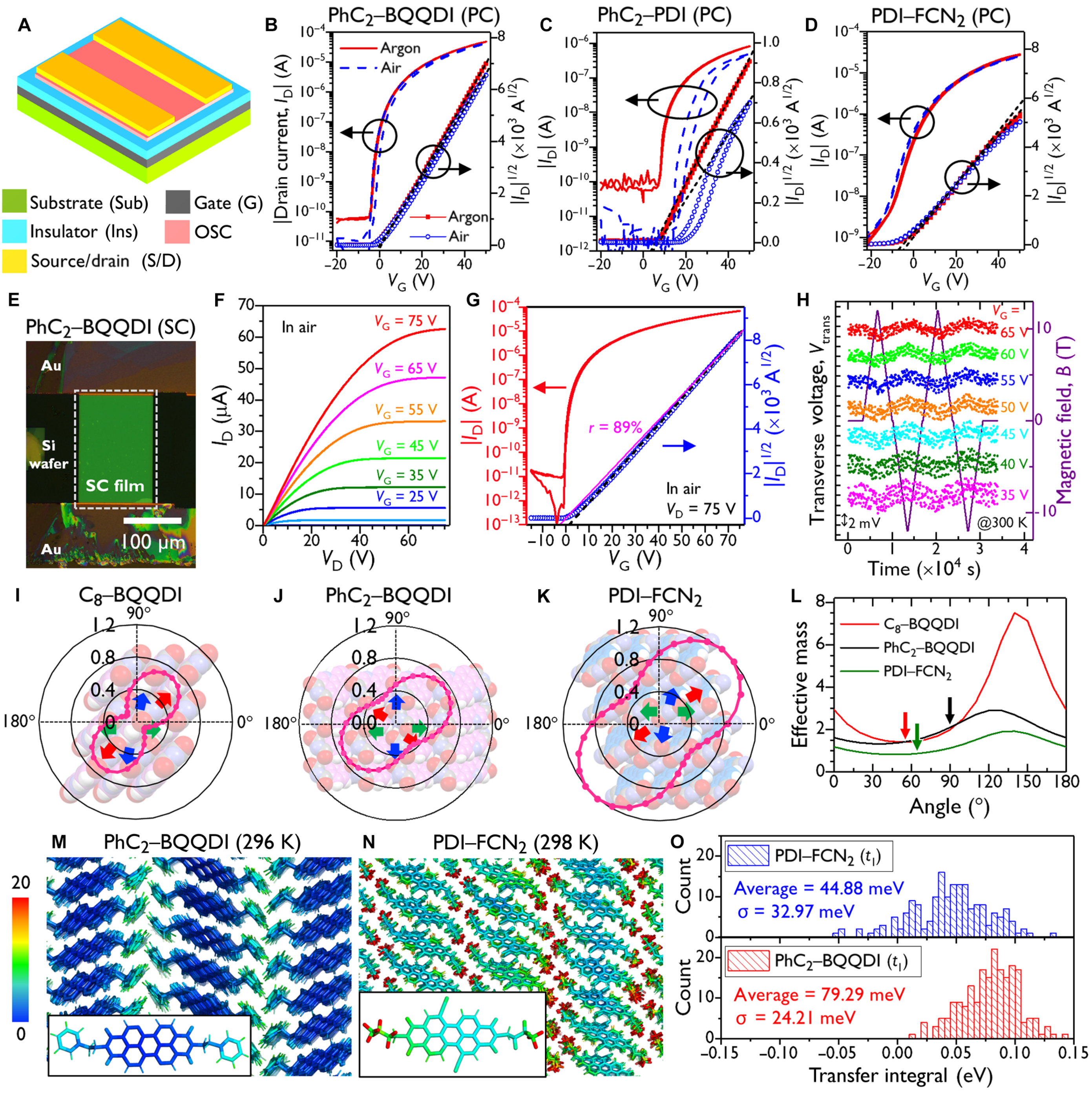

Fig. 5. TFT evaluations and theoretical analyses. (**A**) General TFT structure used in this work. Details of the components are described in the respective captions. (**B** to **D**) Transfer characteristics of PC-TFTs [Sub = G = n^{++}-Si; Ins = SiO$_2$ (200 nm) + DTS-SAM, C_i = 17.3 nF cm^{-2}; S/D = Au (40 nm)] based on PhC$_2$–BQQDI, PhC$_2$–PDI, and PDI–FCN$_2$, respectively. Red and blue symbols indicate data acquired under Ar and ambient air, respectively. Black dashed lines fit the square root of drain current ($|I_D|^{1/2}$), allowing μ_e to be estimated. (**E**) A polarized microscopy image of a PhC$_2$–BQQDI SC-TFT (L = 190 μm, W = 136 μm) [Sub = G = n^{++}-Si; Ins = SiO$_2$ (200 nm) + AL-X601 (60 nm), C_i = 12.5 nF cm^{-2}; S/D = Au (40 nm)]. (**F**) The corresponding output characteristics and (**G**) transfer characteristic (V_D = 75 V). Black dashed and magenta solid lines represent the fit to $|I_D|^{1/2}$ and the slope of an electrically equivalent ideal TFT (41). (**H**) Gated Hall effect data obtained from a PhC$_2$–BQQDI SC-TFT at 300 K. At $V_G \geq 35$ V, the transverse voltage (V_{trans}, colored dots) was modulated using an applied magnetic field (B, purple solid line). (**I**) Packing structures in the *ac*- and *ab*-planes with estimation of the inverses of effective masses for C$_8$–BQQDI. (**J**) Packing structures in the *bc*- and *ab*-planes with estimates for the inverses of effective masses for PhC$_2$–BQQDI. (**K**) Packing structures in the *bc*- and *ab*-planes with estimates of the inverses of effective mass for PDI–FCN$_2$. (**L**) Angle-resolved effective masses for C$_8$–BQQDI, PhC$_2$–BQQDI, and PDI–FCN$_2$. Arrows indicate the channel directions of the SC-TFTs evaluated in this work. (**M** and **N**) Color-coded B-factor distributions (unit: Å^2 s^{-1}) for PhC$_2$–BQQDI and PDI–FCN$_2$ obtained from the trajectories during the last 20 ns of a 100-ns MD run. (**O**) Statistical distributions of intermolecular transfer integrals (t_1) at 100 ns for PhC$_2$–BQQDI and PDI–FCN$_2$. The magnitude of the dynamic fluctuations of t_1 can be evaluated based on the SD (σ). The effective mass is shown in unit of the rest mass of an electron.

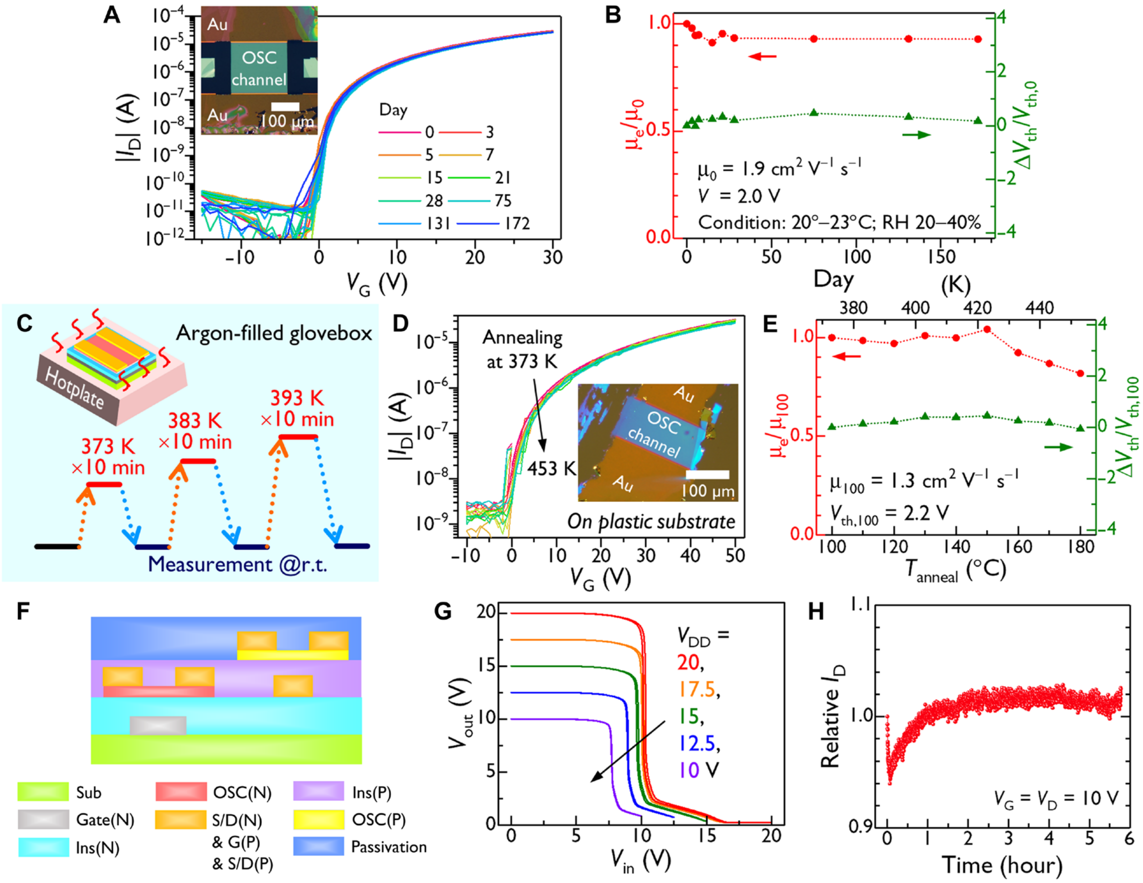

Fig. 6. Practical applicability of PhC$_2$–BQQDI SC-TFTs. (**A**) Transfer curves ($V_D = 30$ V) and (**B**) time-dependent μ_e and V_{th} shift (ΔV_{th}) values normalized relative to those in the as-prepared state (μ_0 and $V_{th,0}$, respectively) acquired during ambient shelf-life tests. Inset in (A) shows a top-view polarized optical micrography image of the TFT. TFT structure: Sub = G = n^{++}-Si; Ins = SiO$_2$ (100 nm) + β–PTS-SAM, $C_i = 34.5$ nF cm^{-2}; S/D = Au (40 nm). $L = 188$ μm, $W = 216$ μm. RH, relative humidity. (**C**) Schematic summarizing the experimental process. (**D**) Transfer curves ($V_D = 50$ V) and (**E**) μ_e and ΔV_{th} values normalized relative to those after annealing at 100°C (μ_{100} and $V_{th,100}$, respectively) as a function of annealing temperature (T_{anneal}). Inset in (D) shows a top-view polarized optical micrography image of the TFT. TFT structure: Sub = polycarbonate (120 μm); G = Au (40 nm); Ins = AL-X601 (260 nm), $C_i = 10.2$ nF cm^{-2}; S/D = Au (40 nm). $L = 98$ μm, $W = 210$ μm. (**F**) Schematic diagram of the CMOS device. Detailed information about the device structure is given in the Supplementary Materials. (**G**) Voltage transfer curves obtained from a CMOS inverter. (**H**) Gate-bias stress values obtained in air for the PhC$_2$–BQQDI TFT having the structure shown in (F).

or at the crystal-substrate interface (*44*). The thermal stress tests were performed using a TFT prepared from a polycarbonate substrate that has a high glass-transition temperature (above 200°C). As shown in Fig. 6 (C to E), both μ_e and V_{th} remained nearly unchanged up to 180°C. Unexpectedly, no performance variation was found when a silicon substrate was used, indicating the applicability of this compound to both plastic and more robust substrates (fig. S27). Note that the mobility of PhC$_2$–BQQDI on the plastic substrate device was 1.3 cm^2 V^{-1} s^{-1}, which is lower than values obtained on silicon wafer substrates because of the roughness of plastics, a greater concentration of populated interface traps, and/or thickness or morphology of the SC-TFT.

Unlike silicon electronics, the fine patterning of organic TFTs by photolithography to fabricate practical, highly integrated electronic circuits has not been demonstrated often because of chemical compatibility issues. However, the chemical robustness of PhC$_2$–BQQDI enabled a CMOS device to be produced via photolithography combined with large-area solution processing (*45*–*47*) to form thin-film crystals using a 0.03 weight % (wt %) solution in 1-chloronaphthalene (solubility, 0.038 wt % at 150°C). The solution-coating process was conducted at 140 to 150°C. As a result, PhC$_2$–BQQDI–based TFTs with channel length and width values of 10 and 500 μm were integrated with sophisticated p-type OSC-based TFTs (Fig. 6F and fig. S31A). This device underwent a full rail-to-rail swing CMOS inverter operation (Fig. 6G). In addition, using this device structure, PhC$_2$–BQQDI exhibited relatively high resistance to gate-bias stress in air, with only <6% deviation over 6 hours (Fig. 6H).

Conclusions and outlook

The design of a nitrogen-containing π-electron framework, BQQDI, based on highly unique molecular design strategies was described. The BQQDI framework enhances the intermolecular orbital overlaps by introducing electronegative N atoms at the optimum position of the π-electron system and the minimum number of electron-withdrawing groups that effectively function for structural control between molecules. This is an unprecedented molecular skeleton with high charge-transport ability owing to enhanced molecular orbital overlaps between adjacent molecules and effectively suppressed molecular motions, high atmospheric stability, and high structural stability. The present n-type OSCs substantially advance high-end organic-based electronics.

MATERIALS AND METHODS

Material preparation

Details of syntheses and characterizations can be found in the Supplementary Materials.

Dimethyl 2,2′-(9,10-dioxo-9,10-dihydroanthracene-1,5-diyl) bis(2-cyanoacetate) (1)

KO^{t}Bu (150.6 g, 1.34 mol) was added to a mixture of 1,5-dinitroanthraquinone (50 g, 168 mmol) and methyl cyanoacetate (133 ml, 1.34 mol) in dimethyl sulfoxide (600 ml; 0.28 M), and the solution was stirred for 3 hours at 50°C. The reaction was quenched with water and acidified to pH = 1 using 12 M hydrochloric acid to obtain a brown precipitate. The precipitates were filtered and washed with distilled water. The crude products were purified by silica gel column chromatography (CH_2Cl_2:AcOEt = 98:2 as eluent) to afford the target compound **1** as a colorless powder (26.0 g, 64.6 mmol, 38%). Melting point (m.p.): 186.0 to 188.0°C. ^1H nuclear magnetic resonance (NMR) (400 MHz, $CDCl_2CDCl_2$ at 100°C) δ 8.40 (dd, *J* = 7.8 Hz, *J* = 1.4 Hz, 2H), 7.95 (d, *J* = 8.0 Hz, 2H), 7.86 (t, *J* = 7.8 Hz, 2H), 6.16 (d, *J* = 10 Hz, 2H), 3.84 (s, 6H). ^{13}C NMR (100 MHz, $CDCl_2CDCl_2$ at 100°C) δ 184.0, 164.6, 136.4, 136.0, 134.6, 131.8, 129.7, 129.6, 115.2, 53.9, 41.5. Time of flight (TOF) high-resolution mass spectrometry (HRMS) (atmospheric pressure chemical ionization; APCI) calculated for $C_{22}H_{15}N_2O_6$ $[M + H]^+$ 403.0930, found 403.0919. Analysis calculated for $C_{22}H_{14}N_2O_6$: C, 65.67; H, 3.51; N, 6.96, found: C, 65.41; H, 3.76; N, 6.88.

Dimethyl 2,8-dihydroxybenzo[*de*]isoquinolino[1,8-*gh*] quinoline-3,9-dicarboxylate (2)

Compound **1** (23.0 g, 57.2 mmol) was added to concentrated sulfuric acid (230 ml). After stirring for 30 min at room temperature, the solution was poured into distilled water (1900 ml) and stirred at 50°C for 20 min. After addition of 50 wt % sodium hydroxide solution (710 ml), the mixture was stirred an additional 10 min at 80°C. After acidification to pH 7 with concentrated hydrochloric acid, the precipitates obtained were collected by filtration and washed with distilled water and acetone to afford the desired product **2** as an orange solid (20.0 g, 49.7 mmol, 87% yield). m.p.: 242.0°C (from TG-DTA). ^1H NMR (400 MHz, $CDCl_2CDCl_2$ at 100°C): δ 12.4 (br, 2H), 8.93 (d, *J* = 7.2 Hz, 2H), 8.82 (d, *J* = 8.8 Hz, 2H), 7.87 (dd, *J* = 8.4 Hz, *J* = 7.6 Hz, 2H), 4.15 (s, 6H). ^{13}C NMR (100 MHz, $CDCl_2CDCl_2$ at 100°C): δ 171.7, 165.8, 155.1, 137.2, 133.0, 131.5, 128.6, 125.0, 120.4, 98.8, 52.9. TOF HRMS (APCI): calculated for $C_{22}H_{15}N_2O_6$ $[M + H]^+$ 403.0930, found 403.0920. Analysis calculated for $C_{22}H_{14}N_2O_6$: C, 65.67; H, 3.51; N, 6.96, found: C, 65.29; H, 3.73; N, 6.85.

Dimethyl 2,8-bis(((trifluoromethyl)sulfonyl)oxy)benzo[*de*] isoquinolino[1,8-*gh*]quinoline-3,9-dicarboxylate (3)

N-phenylbis(trifluoromethanesulfonimide) (31.7 g, 88.8 mmol, 2.10 equiv.) was added to a mixture of compound **2** (17.0 g, 42.3 mmol), 4-dimethylaminopyridine (516 mg, 4.23 mmol, 0.10 equiv.), and triethylamine (12.8 ml, 93.1 mmol, 2.20 equiv.) in dichloromethane (227 ml) at −20°C under argon gas; the solution was stirred for 2 hours at room temperature. After quenching with a small amount of water, the resulting mixture was concentrated under reduced pressure to obtain a crude material. The crude product was purified by recrystallization from ethyl acetate to afford desired product **3** (20.0 g, 30.0 mmol, 71% yield) as yellow crystals. m.p.: 317.3 to 320.3°C. ^1H NMR (400 MHz, $CDCl_2CDCl_2$ at 100°C): δ 8.84 (d, *J* = 7.2 Hz, 2H), 8.39 (d, *J* = 8.0 Hz, 2H), 7.96 (t, *J* = 8.0 Hz, 2H), 4.11 (s, 6H). ^{13}C NMR (100 MHz, $CDCl_2CDCl_2$ at 100°C): δ 163.4, 151.3, 150.7, 137.4, 133.6, 130.8, 128.8, 127.7, 123.4, 118.9 (q, *J* = 320 Hz), 114.4, 53.1. TOF HRMS (APCI): calculated for $C_{24}H_{13}F_6N_2O_{10}S_2$ $[M + H]^+$ 666.9916, found 666.9913. Analysis calculated for $C_{24}H_{12}F_6N_2O_{10}S_2$: C, 43.25; H, 1.81; N, 4.20, found: C, 43.23; H, 2.15; N, 4.21.

Dimethyl benzo[*de*]isoquinolino[1,8-*gh*]quinoline-3,9-dicarboxylate (4)

A mixture of compound **3** (20.0 g, 30.0 mmol), $Pd(PPh_3)_4$ (3.47 g, 3.00 mmol, 0.10 equiv.), triethylamine (25.1 ml, 180 mmol, 6.0 equiv.), formic acid (6.79 ml, 180 mmol, 6.0 equiv.), and *N*,*N*′-dimethylformamide (250 ml) was stirred at 80°C for 2 hours. After cooling to room temperature, the mixture was poured i006Eto distilled water (1000 ml). The precipitates were collected by filtration and washed with distilled water and acetone to afford desired product 4 as a yellow powder (9.17 g, 24.8 mmol, 83% yield). m.p.: 299.5 to 310.0°C. ^1H NMR (400 MHz, $CDCl_2CDCl_2$ at 100°C): δ 9.24 (s, 2H), 9.02 (d, *J* = 7.2 Hz, 2H), 8.97 (d, *J* = 8.4 Hz, 2H), 7.88 (t, *J* = 8.0 Hz, 2H), 4.04 (s, 6H). ^{13}C NMR (100 MHz, $CDCl_2CDCl_2$ at 100°C): δ 166.6, 153.7, 148.0, 134.8, 132.2, 131.9, 128.2, 126.4, 123.7, 120.0, 52.2. TOF HRMS (APCI): calculated for $C_{22}H_{15}N_2O_4$ $[M + H]^+$ 371.1032, found 371.1035. Analysis calculated for $C_{22}H_{14}N_2O_4$: C, 71.35; H, 3.81; N, 7.56, found: C, 71.19; H, 3.84; N, 7.48.

Dimethyl 4,10-dibromobenzo[*de*]isoquinolino[1,8-*gh*] quinoline-3,9-dicarboxylate (5)

To a solution of compound **4** (4.00 g, 10.8 mmol) in concentrated sulfuric acid (50 ml) was added *N*-bromosuccimide (NBS) (14.4 g, 81.0 mmol, 7.5 equiv.) at room temperature. The mixture was stirred at 50°C for 2.5 hours. The resulting mixture was poured into ice water (500 ml), followed by neutralization with 50/100 w/v sodium hydroxide solution. The precipitates were collected by filtration and washed with distilled water and acetone. The solid obtained was purified by silica gel column chromatography (THF:dichloromethane = 1:99) to afford desired product 5 as a yellow solid (2.70 g, 5.11 mmol, 47% yield). m.p.: 272.0 to 274.0°C. ^1H NMR (400 MHz, $CDCl_2CDCl_2$ at 100°C): δ 8.84 (d, *J* = 8.4 Hz, 2H), 8.70 (s, 2H), 8.13 (d, *J* = 8.0 Hz, 2H), 4.02 (s, 6H). ^{13}C NMR (100 MHz, $CDCl_2CDCl_2$ at 100°C): δ 168.2, 151.6, 145.2, 137.8, 132.2, 131.4, 127.0, 125.6, 124.8, 122.1, 53.0. TOF HRMS (APCI): calculated for $C_{22}H_{13}Br_2N_2O_4$ $[M + H]^+$ 526.9242, found 526.9232. Analysis calculated for $C_{22}H_{12}Br_2N_2O_4$: C, 50.03; H, 2.29; N, 5.30, found: C, 49.76; H, 2.61; N, 5.25.

3,9-Dimethyl 10,4-bis(2,4,6-trichlorophenyl)benzo[*de*] isoquinolino[1,8-*gh*]quinoline-3,4,9,10-tetracarboxylate (6)

Compound **5** (1.40 g, 2.65 mmol), 2,4,6-trichlorophenyl formate (2.53 g, 10.6 mmol), $Pd(OAc)_2$ (59.5 mg, 0.265 mmol, 0.10 equiv.), Xantphos (307 mg, 0.530 mmol, 0.20 equiv.), and toluene (13.7 ml) were charged to a Schlenk tube. The mixture was degassed and filled with argon. Triethylamine (1.47 ml, 10.6 mmol, 4.0 equiv.) was added to the reaction mixture, followed by stirring at 100°C for 12 hours. After cooling to room temperature, the mixture was poured into distilled water and extracted with chloroform. The organic layer was dried over magnesium sulfate. After concentration under reduced pressure, the crude product was purified by column chromatography (using chloroform as an eluent) to afford desired product **6** as a yellow solid (410 mg, 0.502 mmol, 22% yield). m.p.: 283.9 to 285.4°C (decomposition). ^{1}H NMR (400 MHz, $CDCl_2CDCl_2$ at 100°C): δ 9.26 (d, *J* = 7.6 Hz, 2H), 9.12 (s, 2H), 8.91 (d, *J* = 7.6 Hz, 2H), 7.46 (s, 4H), 3.91 (s, 6H). ^{13}C NMR (100 MHz, $CDCl_2CDCl_2$ at 100°C): δ 167.0, 162.5, 151.4, 147.3, 143.1, 136.6, 135.9, 132.5, 132.3, 130.0, 128.9, 127.5, 126.0, 124.7, 124.3, 52.8. TOF HRMS (APCI): calculated for $C_{36}H_{17}Cl_6N_2O_8$ $[M + H]^+$ 814.9116, found 814.9094. Analysis calculated for $C_{36}H_{16}Cl_6N_2O_8$: C, 52.91; H, 1.97; N, 3.43, found: C, 52.81; H, 2.07; N, 3.39.

3,4,9,10-Benzo[*de*]isoquinolino[1,8-*gh*]quinolinetetracarboxylic dianhydride (BQQ-TCDA)

To a solution of compound **6** (3.00 g, 3.67 mmol) in *o*-dichlorobenzene (*o*DCB) (0.02 M) was added *p*-TsOH·H_2O (1.81 g, 9.54 mmol, 2.6 equiv.) and the solution heated at 120°C for 24 hours. After cooling to room temperature, the reddish suspension was filtered and the precipitate washed with ethyl acetate until the filtrate became colorless. After drying in vacuo, the desired compound (BQQ–TCDA) was obtained as a red-orange powder (1.29 g, 3.27 mmol, 89%). m.p.: >350°C. ^{1}H NMR (400 MHz, $CDCl_2CDCl_2$ at 100°C): δ 9.70 (s, 2H), 9.35 (d, *J* = 7.6 Hz, 2H), 8.91 (d, *J* = 7.6 Hz, 2H). ^{13}C NMR spectrum was not obtained because of poor solubility. TOF HRMS (APCI): calculated for $C_{22}H_7N_2O_6$ $[M + H]^+$ 395.0304, found 395.0300. Analysis calculated for $C_{22}H_6N_2O_6$: C, 67.02; H, 1.53; N, 7.10, found: C, 67.17; H, 1.61; N, 7.28.

General synthesis of BQQDI derivatives (R = PhC_2, C_8)

A mixture of BQQ–TCDA (0.03 M), the selected amine (2.6 to 3.0 equiv.), and propionic acid (100 equiv.) in *o*DCB was stirred at 150°C for 11 to 15 hours under argon atmosphere. After cooling to room temperature, an excess amount of MeOH was added to the reaction mixture to obtain a crude precipitate, which was collected by suction filtration. The crude product was either recrystallized or sublimed more than once to afford the desired elementally pure device-grade compounds.

N,N′-Diphenethyl-3,4,9,10-benzo[*de*]isoquinolino[1,8-*gh*]quinolinetetracarboxylic diimide (PhC_2–BQQDI)

Reaction period was 15 hours and resulted in a crude yield of 99%. Purification was achieved using sublimation, which yielded 84% of a shiny brown solid. m.p.: >350°C. ^{1}H NMR (400 MHz, $CDCl_2CDCl_2$ at 100°C): δ 9.66 (s, 2H), 9.29 (d, *J* = 7.6 Hz, 2H), 8.85 (d, *J* = 7.6 Hz, 2H), 7.35–7.27 (m, 8H), 7.20 (m, 2H), 4.45 (td, *J* = 8.0 Hz, *J* = 2.2 Hz, 4H), 3.08 (td, *J* = 7.8 Hz, *J* = 2.0 Hz, 4H). ^{13}C NMR spectrum could not be obtained because of poor solubility. TOF HRMS (APCI): calculated for $C_{38}H_{25}N_4O_4$ $[M + H]^+$ 601.1876, found 601.1868. Analysis calculated for $C_{38}H_{24}N_4O_4$: C, 75.99; H, 4.03; N, 9.33, found: C, 75.72; H, 4.12; N, 9.23. Plate-shaped red-orange single crystals of PhC_2–BQQDI were grown from nitrobenzene under ambient atmosphere. The single crystal obtained was measured at 296 K. A total of 15,180 reflections were measured at the maximum 2θ angle of 68.2°, of which 2504 were independent reflections (R_{int} = 0.0289). Analysis was conducted with a space group of $P2_1/n$ without disorder expediently. Crystal structure data are as follows: $C_{38}H_{24}N_4O_4$; formula weight (FW) = 600.61, Monoclinic, $P2_1/n$, $a = 7.7048(2)$ Å, $b = 5.02249(15)$ Å, $c = 35.8104(11)$ Å, β = 92.467(7)°, $V = 1384.48(7)$ Å^3, $Z = 2$, $D_{calcd} = 1.441$ g cm^{-3}, $F(000) = 624.0$, μ = 0.771 (mm^{-1}), refinement converged to R_1 $[I > 2\sigma(I)] = 0.0443$, w$R_2$ (all data) = 0.1229, and the goodness-of-fit (GOF) = 1.105 (CCDC-1938483). A larger single crystal suitable for analysis at 373 K was obtained from 1:1 (v/v) nitrobenzene:1-methylnaphthalene [1:1 (v/v)]. At 373 K, a total of 5657 reflections were measured at the maximum 2θ angle of 73.25°, of which 2537 were independent reflections (R_{int} = 0.0204). Crystal structure data are as follows: $C_{38}H_{24}N_4O_4$; FW = 600.61, Monoclinic, $P2_1/n$, $a = 7.71527(18)$ Å, $b = 5.04433(12)$ Å, $c = 35.9921(10)$ Å, β = 92.202(2)°, $V = 1399.72(6)$ Å^3, $Z = 2$, $D_{calcd} = 1.425$ g cm^{-3}, $F(000) = 624.0$, μ = 0.763 (mm^{-1}), refinement converged to R_1 $[I > 2\sigma(I)] = 0.0432$, w$R_2$ (all data) = 0.1222, and GOF = 1.059 (CCDC-1938480).

N,N′-Dioctyl-3,4,9,10-benzo[*de*]isoquinolino[1,8-*gh*]quinolinetetracarboxylic diimide (C_8–BQQDI)

Reaction period was 11 hours and resulted in a crude yield of 93%. Purification was achieved using recrystallization of crude product from *o*DCB, sublimation and then recrystallization from *o*DCB. Purification yielded 50% of a red-orange solid. m.p.: >350°C. ^{1}H NMR (400 MHz, $CDCl_2CDCl_2$ at 100°C): δ 9.64 (s, 2H), 9.27 (d, *J* = 8.0 Hz, 2H), 8.83 (d, *J* = 7.6 Hz, 2H), 4.20 (t, *J* = 7.4 Hz, 4H), 1,78 (m, 4H), 1.48–1.26 (m, 20H), 0.88 (t, *J* = 7.0 Hz, 6H). ^{13}C NMR spectrum could not be obtained because of poor solubility. TOF HRMS (APCI): calculated for $C_{38}H_{41}N_4O_4$ $[M + H]^+$ 617.3128, found 617.3119. Analysis calculated for $C_{38}H_{40}N_4O_4$: C, 74.00; H, 6.54; N, 9.08, found: C, 73.91; H, 6.56; N, 9.00. Plate-shaped orange single crystals of C_8–BQQDI were grown by recrystallization from 2-chlorotoluene under ambient atmosphere. The single crystal obtained was measured at 300 K. A total of 9400 reflections were measured at the maximum 2θ angle of 68.175°, of which 2829 were independent reflections (R_{int} = 0.1030). Analysis was conducted with a space group of $P\bar{1}$ without disorder expediently. Crystal structure data are as follows: $C_{38}H_{40}N_4O_4$; FW = 616.74, Triclinic, $P\bar{1}$, $a = 4.7101(4)$ Å, $b = 6.6707(6)$ Å, $c = 26.091(2)$ Å, α = 87.686(6)°, β = 89.709(6)°, γ = 74.785(5)° $V = 790.38(12)$ Å^3, $Z = 1$, $D_{calcd} = 1.296$ g cm^{-3}, $F(000) = 328.0$, μ = 0.677 (mm^{-1}), refinement converged to R_1 $[I > 2\sigma(I)] = 0.0869$, w$R_2$ (all data) = 0.2177, and GOF = 0.946 (CCDC-1938481).

N,N′-Di(4-heptyl)-3,4,9,10-benzo[*de*]isoquinolino[1,8-*gh*]quinolinetetracarboxylic diimide (4-Hep–BQQDI)

A mixture of BQQ – TCDA (0.30 g, 0.76 mmol), 4-heptylamine (0.91 ml, 5.70 mmol, 7.5 equiv.) and propionic acid (5.7 ml, 76 mmol, 100 equiv.) in *o*DCB (25 ml, 0.03 M) was heated at 150°C for 38 hours. After cooling to room temperature, the suspension was filtered through Celite and washed with chloroform until the filtrate became colorless. The filtrates were collected and concentrated under reduced pressure to afford a red-brown solid (0.096 g). Purification by gel permeation chromatography afforded the desired product as an orange solid (0.045 g, 0076 mmol, 10%). m.p.: >343°C (decomposition). ^{1}H NMR (400 MHz, $CDCl_3$ at 30°C): δ 9.57 (s, 2H), 9.16 (d, *J* = 8.0 Hz, 2H), 8.79 (d, *J* = 7.6 Hz, 2H), 5.23 (m, 2H), 2.31–2.21 (m, 4H), 1.90–1.80 (m, 4H), 0.94 (t, *J* = 7.4 Hz, 12H). ^{13}C NMR (100 MHz, $CDCl_3$ at 30°C): δ 160.3 (br), 149.4, 145.6 (br), 132.1, 131.8 (br), 128.8, 123.9, 121.3 (br), 118.7, 113.8 (br), 51.4, 31.5, 17.1, 10.9. A lack of one ^{13}C signal was likely due to two broad signals assignable to the carbonyl carbons [160.3 parts per million (ppm)] that overlapped. TOF HRMS (APCI): calculated for $C_{36}H_{37}N_4O_4$ $[M + H]^+$ 589.2815, found 589.2805. Analysis calculated for $C_{36}H_{36}N_4O_4$: C, 73.45; H, 6.16; N, 9.52, found: C, 73.15; H, 6.26; N, 9.26.

Computational calculations

The LUMOs of the Me–BQQDI and Me–PDI molecules were obtained by density functional theory (DFT) at the B3LYP/6–31 + G(d) level of theory using Spartan 16, Wavefunction Inc.

The intermolecular interaction energies between pairs of adjacent molecules were obtained at the M06-2X/6–31++G(d,p) level of DFT (*48*) with counterpoise correction (*49*, *50*) for the basis set superposition error. Results of this level of calculation were very similar to those obtained using the higher-level DFT method MP2/6–31++G(d,p).

Transfer integrals between LUMOs of neighboring molecules were calculated using the dimer method (*6*) at the PBEPBE/6-31G(d) level of DFT (*50*). Atomic coordinates were obtained from the experimental single-crystal structures or the MD simulations.

LUMO band structures, $E(k)$, were calculated by the tight-binding approximation using transfer integrals. Effective masses of electrons were calculated as $m^* = \hbar^2 \left(\frac{\partial^2 E(k)}{\partial k^2}\right)^{-1}$ along the respective directions.

Instrumental characterizations

Cyclic voltammetry (CV) was conducted using a BAS electrochemical analyzer (ALS 622D) in conjunction with a three-electrode cell incorporating a glassy carbon as the working electrode, a Pt wire as the counter electrode, and 0.01 M Ag/AgNO$_3$ [in benzonitrile containing 0.1 M tetrabutylammonium hexafluorophosphate (TBAPF$_6$)] as the reference electrode. The measurements were conducted under an argon atmosphere using a 0.5 mM benzonitrile solution of the test compound and 0.1 M TBAPF$_6$ as a supporting electrolyte, at a scan rate of 0.1 V s^{-1}. The redox potentials were calibrated using ferrocene (Fc; E(Fc/Fc$^+$) = 0 V) as an internal standard. Before the CV trials, the benzonitrile was purified by passing through a pad of aluminum oxide 60 (Merck). TG-DTA data were acquired using a Rigaku Thermo Plus EVO II TG 8121 instrument at a heating rate of 1 K min^{-1} under a nitrogen flow (100 ml min^{-1}). The UV-vis absorption spectra were recorded with a Jasco V-670 spectrometer. Vacuum-deposited 100-nm-thick films were prepared on synthetic quartz substrates at a deposition rate of 0.5 Å s^{-1} at room temperature. Time-dependent UV-vis spectra of both the solutions and films were acquired in ambient air with sample storage under room light. Atomic force microscope images were obtained using a Shimadzu SPM-9700HT instrument in a dynamic mode. Thickness of the AL-X601 layer was measured using a Bruker DektakXT profilemeter. Thin-film x-ray diffraction profiles were collected by 2θ/ω scan on a Rigaku SmartLab diffractometer with a Cu*K*α source (λ = 1.54056 Å).

Single-crystal x-ray diffraction

Single-crystal x-ray diffraction data were collected on either a Rigaku R-AXIS RAPID II imaging plate diffractometer with Cu*K*α radiation (λ = 1.54187 Å) or a Rigaku XtaLAB Synergy-Custom instrument with Cu*K*α radiation (λ = 1.54184 Å) at room temperature. The structures were solved by direct methods [SHELXT (2015)] and refined by full-matrix least-squares procedures on F2 for all reflections [SHELXL (version 2014/7) or SHELXL (version 2018/3)]. While all hydrogen atoms were placed using AFIX instructions, all other atoms were refined anisotropically. Crystallographic data have been deposited in the Cambridge Crystallographic Data Centre (CCDC) as a supplementary publication. These data can be obtained free of charge at www.ccdc.cam.ac.uk/data_request/cif.

Vacuum-deposited PC-TFT fabrications

Preparations of the PC-TFTs were carried out under ambient air unless stated otherwise. Vacuum-deposited 40-nm-thick PC thin films were used to produce top-contact, bottom-gate TFTs. In preparation for fabrication, a highly n^{++}-doped silicon wafer with a thermally grown SiO$_2$ layer (200 nm) was washed by ultrasonication in acetone and isopropanol. After drying on a hotplate in air, the wafer was treated with UV–O$_3$ and then exposed to decyltrimethoxysilane (DTS) vapor at 130°C to produce a self-assembled monolayer (SAM). After washing in acetone and isopropanol again, OSCs were vacuum-deposited at a rate of 0.3 to 0.5 Å s^{-1} to form 40-nm-thick PC films, during which the substrates were kept at 140°C. A gold coating was subsequently vacuum-evaporated through a shadow mask to obtain 60-nm-thick source and drain electrodes. Typical channel length (L) and width (W) values were 200 and 1000 μm, respectively. Before evaluation, the TFTs were thermally annealed at 100°C for 2 hours in an argon-filled glovebox.

Solution-deposited SC-TFT fabrications

Device preparation processes were performed under ambient air if not stated otherwise. The solution-processed SC-TFTs were analyzed using either highly n^{++}-doped silicon wafers or polycarbonate films as substrates. The surfaces of the silicon wafers were treated with a fluorinated insulating polymer, AL-X601 (*13*, *51*) (AGC Inc.), or a SAM of trimethoxy(2-phenylethyl)silane (β–PTS). In both cases, a highly n^{++}-doped silicon wafer with a thermally grown SiO$_2$ layer (100 or 200 nm) was ultrasonicated in acetone and isopropanol and then dried on a hotplate in air. Following UV–O$_3$ treatment, either a solution of AL-X601 in propylene glycol monomethyl ether acetate was spin-coated onto the wafer and cured at 150°C for 30 min in air or the wafer was exposed to β–PTS vapor at 120°C for 3 hours. The polycarbonate substrates were used only for thermal stress studies. A 120-μm-thick polycarbonate film (SS120, Teijin Limited) was first cured at 200°C followed by the application of a thick AL-X601 layer by spin coating for surface smoothing. Subsequently, a gate electrode was formed by generating a 40-nm-thick gold layer via thermal evaporation. Following this, an approximately 260-nm-thick AL-X601 layer was formed by spin coating followed by cross-linking at 150°C for 20 min and then further curing at 180°C for 10 min.

The SC-TFTs were investigated using bottom-gate, top-contact TFT structures. The SC thin films used in these devices were fabricated by a solution-processing technique known as the edge-casting method (*40*). Crystalline thin films of PhC$_2$–BQQDI, C$_8$–BQQDI and PDI–FCN$_2$ were grown from a 0.03 wt % 1-methylnaphthalene solution at 130°C, a 0.1 wt % 1-methylnaphthalene at 110°C, and a 0.1 wt % butyl phenyl ether solution at 115°C, respectively. After crystallization was complete, the crystals were dried thoroughly in a vacuum oven at 100°C for 10 hours. Following this, 40-nm-thick gold layers were vacuum-deposited through a metal shadow mask to produce source and drain electrodes. Objective channel regions were edged using a conventional Nd:YAG laser etching technique or formed manually using cotton swabs. Before measurements, thermal annealing was performed at 80 to 100°C for 2 to 24 hours to remove residual water and to improve the gold electrode–semiconductor contacts, both of which resulted in improved TFT performance.

Device evaluations

Electrical evaluations of the TFTs were conducted on a Keithley 2634B SourceMeter and a Keithley 4200-SCS semiconductor parameter analyzer in an Ar-filled glovebox ([O$_2$] < 1 ppm, [H$_2$O] < 3 ppm) and in an ambient air (20 to 23°C, relative humidity 20 to 40% unless stated otherwise), respectively. For AL-X601-containing gate dielectrics, gate capacitance per unit area (C_i) was estimated using a Toyo FCE-3 ferroelectric test system on the metal-insulator-metal structure. Electron mobility and threshold voltage values were extracted from the transfer characteristics based on the conventional equation for the saturation regime

$$\sqrt{|I_D|} = \sqrt{\frac{W\mu_e C_i}{2L}}(V_G - V_{th})$$

where I_D is the drain current, W is the channel width, μ_e is the electron mobility, C_i is the gate capacitance per unit area, L is the channel length, V_G is the gate voltage, and V_{th} is the threshold voltage.

Stress durability tests on TFTs

To assess long-term atmospheric stability, devices were stored under ambient conditions for various times, after which TFT evaluations were conducted in air. Thermal stress tests were performed in an Ar-filled glovebox by transferring SC-TFTs that were prepared in air. Thermal treatments were carried out on a hotplate at temperatures from room temperature to the desired annealing temperature (T_{anneal}), which was then held for 10 min. The sample was then allowed to cool naturally to room temperature followed by TFT evaluations conducted at room temperature.

Determination of crystallographic axes of solution-deposited single-crystal films

To determine the crystallographic axes of the thin-film single crystals, x-ray diffraction analyses were carried out with a Rigaku R-AXIS RAPID II imaging plate diffractometer with a Cu$K\alpha$ radiation (λ = 1.54187 Å) at room temperature. The ω scans at appropriate χ angles were conducted around ω = 0°, which corresponds to x-ray irradiation parallel to the substrate surface.

Gated Hall effect measurement

The gated Hall effect measurement was conducted on a solution-deposited SC-TFT. Details of device preparation and analysis can be found in the Supplementary Materials.

CMOS device fabrication and characterizations

The integrated CMOS device was fabricated on a 10 cm by 10 cm piece of supporting glass. This support was laminated with a polyimide film (Xenomax, Toyobo Co., Ltd.), followed by spin coating and patterning by conventional photolithography of silver ink to produce a substrate (Sub) with a gate electrode [Gate(N)]. The photolithography was performed using AZ5214E (MicroChemicals GmbH) as photoresist and SEA-1 (KANTO Chemical Co. Inc.) as etchant. Then, alumina (50 nm) and AL-X601 (50 nm) layers were formed by atomic layer deposition (ALD) and spin-coating, respectively, to produce a gate insulator [Ins(N)]. A large-area PhC_2–BQQDI SC film was formed using the continuous edge-casting printing method (*46*) with a 0.03 wt % 1-chloronaphthalene solution at 145 to 150°C. Then, a PhC_2–BQQDI layer [OSC(N)] and 100-nm-thick Au electrodes working as both S/D(N) and G(P) were patterned by multiple photolithographic processes, where OSCoR4001 (Orthogonal Inc.) and AURUMS-50790 (KANTO Chemical Co. Inc.) were used as a photoresist and gold etchant, respectively, while the OSC was dry-etched by reactive ion etching under an O_2 flow (50 W, 250 mTorr). The diX-SR (Kisco Ltd.) (25 nm), alumina (50 nm), and diX-SR (25 nm) layers were fabricated sequentially, using chemical vapor deposition (CVD) and ALD for the alumina and diX-SR, respectively, to form the trilayer Gate(P). The continuous edge-casting printing of 3,11-dinonyldinaphtho[2,3-*d*:2′,3′-*d*′]benzo[1,2-*b*:4,5-*b*′]dithiophene (C_9–DNBDT–NW) from a 0.02 wt % solution in 3-chlorothiophene afforded a large-area crystalline thin film (*47*). The C_9–DNBDT–NW [OSC(P)] and Au [S/D(P)] layers were patterned by multiple photolithographic processes corresponding to those for OSC(N) and S/D(N). Last, a 1-μm-thick diX-SR passivation layer was formed by CVD. Details of device fabrication will be reported elsewhere. The C_i was 40 nF cm^{-2} for both the *n*- and *p*-channel TFTs. While channel lengths were 10 μm for both channels, the widths were 500 and 50 μm for the *n*- and *p*-channels, respectively. Electrical evaluations of the TFTs and the CMOS inverter were performed using a Keithley 4200-SCS instrument under ambient conditions. The bias stress was monitored with this same instrument under ambient air, applying a constant V_G and V_D of 10 V while recording I_D at 10-s intervals.

MD simulations

All MD simulations of single crystals of the series of organic compounds proposed in this study were conducted using the GROMACS 2016.3 program. Since the intra- and interatomic interactions should be treated explicitly when analyzing atomistic dynamics, an all-atom model was used in accordance with generalized Amber force field (*52*) parameters. The partial atomic charges of the simulated molecules were calculated using restrained electrostatic potential (*53*) methodology, based on quantum chemical calculations using the 6-31G(d) basis set and using the GAUSSIAN 09 program (*48*). The number of molecules, temperature, and simulated systems are described in table S6. The initial structure for each system was constructed from the single-crystal structure obtained in the experiments. For each system, the pre-equilibration run was performed initially at a specific temperature for 5 ns after minimization of the steepest descent energy. During the pre-equilibration runs, the Berendsen thermostat (*54*) was used to maintain the temperature of the system with relaxation times of 0.2 ps, and the volume of the MD cell was kept constant. Subsequently, the equilibration run was performed using the Nosé-Hoover thermostat (*55*–*57*) and Parrinello-Rahman barostat (*58*) with relaxation times of 1.0 and 5.0 ps, respectively. During all MD simulations, the time step was set to 2 fs since all bonds connected to hydrogen atoms were constrained with the LINCS (*59*) algorithm. The pressure of the system was kept at 1.0 bar. The smooth particle-mesh Ewald (*60*) method was used to treat the long-range electrostatic interactions, and the real-space cutoff and grid spacing were 1.2 and 0.30 nm, respectively. The van der Waals interactions were calculated with a cut-off of 1.2 nm. The initial size of the MD cell did not vary significantly (less than 0.5%) during the simulation, and each system reached equilibrium after several tens of nanoseconds. To compare the effect of temperature on the thermal atomic fluctuations of different molecules, the *B*-factors related to the thermal stability were calculated using the following equation

$$B = \frac{8}{3}\pi^2\Delta_i^2$$

where Δ_i is the root mean square fluctuation (RMSF) of atom *i*. The RMSF values, in turn, were estimated from the following relation

$$\Delta_i = \sqrt{\frac{1}{T}\sum_{j=1}^{T}|\boldsymbol{r}_i(t_j) - \bar{\boldsymbol{r}}_i|^2}$$

where T is the time step, $\boldsymbol{r}_i(t_j)$ is the position coordinate of atom i, and $\bar{\boldsymbol{r}}_i$ is the average of $\boldsymbol{r}_i(t_j)$. The RMSF values were analyzed on the basis of MD trajectories during the last 20 ns in the equilibrium stage.

SUPPLEMENTARY MATERIALS

Supplementary material for this article is available at http://advances.sciencemag.org/cgi/content/full/6/18/eaaz0632/DC1

REFERENCES AND NOTES

1. Z. Bao, J. Locklin, *Organic Field-Effect Transistors* (CRC Press, ed. 1, 2007).
2. A. C. Arias, J. D. MacKenzie, I. McCulloch, J. Rivnay, A. Salleo, Materials and applications for large area electronics: Solution-based approaches. *Chem. Rev.* **110**, 3–24 (2010).
3. S.-S. Sun, N. S. Sariciftci, *Organic Photovoltaics: Mechanism, Materials, and Devices* (CRC Press, 2005).
4. K. Müllen, U. Scherf, *Organic Light-Emitting Devices: Synthesis, Properties and Applications* (Wiley-VCH, 2006).
5. J. L. Brédas, J. P. Calbert, D. A. da Silva Filho, J. Cornil, Organic semiconductors: A theoretical characterization of the basic parameters governing charge transport. *Proc. Natl. Acad. Sci. U.S.A.* **99**, 5804–5809 (2002).
6. E. F. Valeev, V. Coropceanu, D. A. da Silva Filho, S. Salman, J.-L. Brédas, Effect of electronic polarization on charge-transport parameters in molecular organic semiconductors. *J. Am. Chem. Soc.* **128**, 9882–9886 (2006).
7. V. Coropceanu, J. Cornil, D. A. da Silva Filho, Y. Olivier, R. Silbey, J.-L. Brédas, Charge transport in organic semiconductors. *Chem. Rev.* **107**, 926–952 (2007).
8. S. Illig, A. S. Eggeman, A. Troisi, L. Jiang, C. Warwick, M. Nikolka, G. Schweicher, S. G. Yeates, Y. Henri Geerts, J. E. Anthony, H. Sirringhaus, Reducing dynamic disorder in small-molecule organic semiconductors by suppressing large-amplitude thermal motions. *Nat. Commun.* **7**, 10736 (2016).
9. A. Troisi, G. Orlandi, J. E. Anthony, Electronic interactions and thermal disorder in molecular crystals containing cofacial pentacene units. *Chem. Mater.* **17**, 5024–5031 (2005).
10. A. Troisi, G. Orlandi, Charge-transport regime of crystalline organic semiconductors: Diffusion limited by thermal off-diagonal electronic disorder. *Phys. Rev. Lett.* **96**, 086601 (2006).
11. S. Ciuchi, S. Fratini, D. Mayou, Transient localization in crystalline organic semiconductors. *Phys. Rev. B* **83**, 081202 (2011).
12. A. S. Eggeman, S. Illig, A. Troisi, H. Sirringhaus, P. A. Midgley, Measurement of molecular motion in organic semiconductors by thermal diffuse electron scattering. *Nat. Mater.* **12**, 1045–1049 (2013).
13. T. Kubo, R. Häusermann, J. Tsurumi, J. Soeda, Y. Okada, Y. Yamashita, N. Akamatsu, A. Shishido, C. Mitsui, T. Okamoto, S. Yanagisawa, H. Matsui, J. Takeya, Suppressing molecular vibrations in organic semiconductors by inducing strain. *Nat. Commun.* **7**, 11156 (2016).
14. H. Ishii, J. Inoue, N. Kobayashi, K. Hirose, Quantitative mobility evaluation of organic semiconductors using quantum dynamics based on density functional theory. *Phys. Rev. B* **98**, 235422 (2018).
15. T. Okamoto, C. Mitsui, M. Yamagishi, K. Nakahara, J. Soeda, Y. Hirose, K. Miwa, H. Sato, A. Yamano, T. Matsushita, T. Uemura, J. Takeya, V-shaped organic semiconductors with solution processability, high mobility, and high thermal durability. *Adv. Mater.* **25**, 6392–6397 (2013).
16. C. Mitsui, T. Okamoto, M. Yamagishi, J. Tsurumi, K. Yoshimoto, K. Nakahara, J. Soeda, Y. Hirose, H. Sato, A. Yamano, T. Uemura, J. Takeya, High-performance solution-processable N-shaped organic semiconducting materials with stabilized crystal phase. *Adv. Mater.* **26**, 4546–4551 (2014).
17. K. Nakahara, C. Mitsui, T. Okamoto, M. Yamagishi, H. Matsui, T. Ueno, Y. Tanaka, M. Yano, T. Matsushita, J. Soeda, Y. Hirose, H. Sato, A. Yamano, J. Takeya, Furan fused V-shaped organic semiconducting materials with high emission and high mobility. *Chem. Commun.* **50**, 5342–5344 (2014).
18. C. Mitsui, H. Tsuyama, R. Shikata, Y. Murata, H. Kuniyasu, M. Yamagishi, H. Ishii, A. Yamamoto, Y. Hirose, M. Yano, T. Takehara, T. Suzuki, H. Sato, A. Yamano, E. Fukuzaki, T. Watanabe, Y. Usami, J. Takeya, T. Okamoto, High performance solution-crystallized thin-film transistors based on V-shaped thieno[3,2-*f*′,4,5-*f*]bis[1]benzothiophene semiconductors. *J. Mater. Chem. C* **5**, 1903–1909 (2017).
19. C. Mitsui, M. Yamagishi, R. Shikata, H. Ishii, T. Matsushita, K. Nakahara, M. Yano, H. Sato, A. Yamano, J. Takeya, T. Okamoto, Oxygen- and sulfur-bridged bianthracene V-shaped organic semiconductors. *Bull. Chem. Soc. Jpn.* **90**, 931–938 (2017).
20. A. Yamamoto, Y. Murata, C. Mitsui, H. Ishii, M. Yamagishi, M. Yano, H. Sato, A. Yamano, J. Takeya, T. Okamoto, Zigzag-elongated fused π-electronic core: A molecular design strategy to maximize charge-carrier mobility. *Adv. Sci.* **5**, 1700317 (2018).
21. T. Okamoto, Next-generation organic semiconductors driven by bent-shaped π-electron cores. *Polym. J.* **51**, 825–833 (2019).
22. H. Iino, T. Usui, J. Hanna, Liquid crystals for organic thin-film transistors. *Nat. Commun.* **6**, 6828 (2015).
23. J.-H. Dou, Y.-Q. Zheng, Z.-F. Yao, T. Lei, X. Shen, X.-Y. Luo, Z.-A. Yu, S.-D. Zhang, G. Han, Z. Wang, Y. Yi, J.-Y. Wang, J. Pei, A cofacially stacked electron-deficient small molecule with a high electron mobility of over 10 $\mathrm{cm^2\,V^{-1}\,s^{-1}}$ in air. *Adv. Mater.* **27**, 8051–8055 (2015).
24. X. Xu, Y. Yao, B. Shan, X. Gu, D. Liu, J. Liu, J. Xu, N. Zhao, W. Hu, Q. Miao, Electron mobility exceeding 10 $\mathrm{cm^2\,V^{-1}\,s^{-1}}$ and band-like charge transport in solution-processed n-Channel organic thin-film transistors. *Adv. Mater.* **28**, 5276–5283 (2016).
25. H. Usta, A. Facchetti, T. J. Marks, n-Channel semiconductor materials design for organic complementary circuits. *Acc. Chem. Res.* **44**, 501–510 (2011).
26. X. Zhan, A. Facchetti, S. Barlow, T. J. Marks, M. A. Ratner, M. R. Wasielewski, S. R. Marder, Rylene and related diimides for organic electronics. *Adv. Mater.* **23**, 268–284 (2011).
27. A. S. Molinari, H. Alves, Z. Chen, A. Facchetti, A. F. Morpurgo, High electron mobility in vacuum and ambient for PDIF-$\mathrm{CN_2}$ single-crystal transistors. *J. Am. Chem. Soc.* **131**, 2462–2463 (2009).
28. S. G. Bucella, A. Luzio, E. Gann, L. Thomsen, C. R. McNeill, G. Pace, A. Perinot, Z. Chen, A. Facchetti, M. Caironi, Macroscopic and high-throughput printing of aligned nanostructured polymer semiconductors for MHz large-area electronics. *Nat. Commun.* **6**, 8394 (2015).
29. T. He, M. Stolte, C. Burschka, N. H. Hansen, T. Musiol, D. Kälblein, J. Pflaum, X. Tao, J. Brill, F. Würthner, Single-crystal field-effect transistors of new $\mathrm{Cl_2}$-NDI polymorph processed by sublimation in air. *Nat. Commun.* **6**, 5954 (2015).
30. B. A. Jones, M. J. Ahrens, M.-H. Yoon, A. Facchetti, T. J. Marks, M. R. Wasielewski, High-mobility air-stable n-type semiconductors with processing versatility: Dicyanoperylene-3,4:9,10-bis(dicarboximides). *Angew. Chem. Int. Ed. Engl.* **43**, 6363–6366 (2004).
31. J. Soeda, T. Uemura, Y. Mizuno, A. Nakao, Y. Nakazawa, A. Facchetti, J. Takeya, High electron mobility in air for *N,N′*-1*H*,1*H*-perfluorobutyldicyanoperylene carboxydi-imide solution-crystallized thin-film transistors on hydrophobic surfaces. *Adv. Mater.* **23**, 3681–3685 (2011).
32. I. Vladimirov, M. Kellermeier, T. Gessner, Z. Molla, S. Grigorian, U. Pietsch, L. S. Schaffroth, M. Küehn, F. May, R. T. Weitz, High-mobility, ultrathin organic semiconducting films realized by surface-mediated crystallization. *Nano Lett.* **18**, 9–14 (2018).
33. Q. Miao, Ten years of N-heteropentacenes as semiconductors for organic thin-film transistors. *Adv. Mater.* **26**, 5541–5549 (2014).
34. M. V. Gorelik, S. P. Titovia, M. A. Kanor, Reaction of α-halogeno- and α-nitroanthraquinones with the anions of CH acids. Part 1. Synthesis of 1-alkyl-, 1,5-dialkyl-, and 1-aroylanthraquinones. *J. Org. Chem. USSR* **28**, 1852–1857 (1992).
35. M. V. Gorelik, S. P. Titovia, M. A. Kanor, Reaction of α-halogeno- and a-nitroanthraquinones with the anions of CH acids. Part 2. Peri-cyclization in the reaction with nitriles. *J. Org. Chem. USSR* **28**, 1858–1864 (1992).
36. H. Konishi, T. Sekino, K. Manabe, Palladium-catalyzed external-CO-free carbonylation of aryl bromides using 2,4,6-trichlorophenyl formate. *Chem. Pharm. Bull.* **66**, 562–567 (2018).
37. T. Steiner, The hydrogen bond in the solid state. *Angew. Chem. Int. Ed.* **41**, 48–76 (2002).
38. U. Zschieschang, K. Amsharov, M. Jansen, K. Kern, H. Klauk, R. T. Weitz, Separating the impact of oxygen and water on the long-term stability of n-channel perylene diimide thin-film transistors. *Org. Electron.* **26**, 340–344 (2015).
39. The parasitic effect and extrinsic factors such as grain boundaries can be neglected.
40. T. Uemura, Y. Hirose, M. Uno, K. Takimiya, J. Takeya, Very high mobility in solution-processed organic thin-film transistors of highly ordered [1]benzothieno[3,2-b]benzothiophene derivatives. *Appl. Phys. Express* **2**, 111501 (2009).
41. H. H. Choi, K. Cho, C. D. Frisbie, H. Sirringhaus, V. Podzorov, Critical assessment of charge mobility extraction in FETs. *Nat. Mater.* **17**, 2–7 (2017).
42. K. Lee, É. D. Murray, L. Kong, B. I. Lundqvist, D. C. Langreth, Higher-accuracy van der Waals density functional. *Phys. Rev. B* **82**, 081101 (2010).
43. S. Fratini, S. Ciuchi, D. Mayou, G. T. de Laissardière, A. Troisi, A map of high-mobility molecular semiconductors. *Nat. Mater.* **16**, 998–1002 (2017).
44. To determine the cause of this behavior and to solve the problem, a study of the annealing condition for the device is underway in our laboratory.
45. J. Soeda, T. Uemura, T. Okamoto, C. Mitsui, M. Yamagishi, J. Takeya, Inch-size solution-processed single-crystalline films of high-mobility organic semiconductors. *Appl. Phys. Express* **6**, 076503 (2013).
46. J. Soeda, T. Okamoto, C. Mitsui, J. Takeya, Stable growth of large-area single crystalline thin films from an organic semiconductor/polymer blend solution for high-mobility organic field-effect transistors. *Org. Electron.* **39**, 127–132 (2016).
47. S. Kumagai, A. Yamamura, T. Makita, J. Tsurumi, Y. Y. Lim, T. Wakimoto, N. Isahaya, H. Nozawa, K. Sato, M. Mitani, T. Okamoto, S. Watanabe, J. Takeya, Scalable fabrication of organic single-crystalline wafers for reproducible TFT arrays. *Sci. Rep.* **9**, 15897 (2019).

48. G. W. T. M. J. Frisch, H. B. Schlegel, G. E. Scuseria, M. A. Robb, J. R. Cheeseman, G. Scalmani, V. Barone, B. Mennucci, G. A. Petersson, H. Nakatsuji, M. Caricato, X. Li, H. P. Hratchian, A. F. Izmaylov, J. Bloino, G. Zheng, J. L. Sonnenberg, M. Hada, M. Ehara, K. Toyota, R. Fukuda, J. Hasegawa, M. Ishida, T. Nakajima, Y. Honda, O. Kitao, H. Nakai, T. Vreven, J. A. Montgomery, J. J. E. Peralta, F. Ogliaro, M. Bearpark, J. J. Heyd, E. Brothers, K. N. Kudin, V. N. Staroverov, T. Keith, R. Kobayashi, J. Normand, K. Raghavachari, A. Rendell, J. C. Burant, S. S. Iyengar, J. Tomasi, M. Cossi, N. Rega, J. M. Millam, M. Klene, J. E. Knox, J. B. Cross, V. Bakken, C. Adamo, J. Jaramillo, R. Gomperts, R. E. Stratmann, O. Yazyev, A. J. Austin, R. Cammi, C. Pomelli, J. W. Ochterski, R. L. Martin, K. Morokuma, V. G. Zakrzewski, G. A. Voth, P. Salvador, J. J. Dannenberg, S. Dapprich, A. D. Daniels, O. Farkas, J. B. Foresman, J. V. Ortiz, J. Cioslowski, D. J. Fox, *Gaussian 09, Revision D. 01* (Gaussian Inc., 2013).
49. S. F. Boys, F. Bernardi, The calculation of small molecular interactions by the differences of separate total energies. Some procedures with reduced errors. *Mol. Phys.* **19**, 553–566 (1970).
50. M. W. Schmidt, K. K. Baldridge, J. A. Boatz, S. T. Elbert, M. S. Gordon, J. H. Jensen, S. Koseki, N. Matsunaga, K. A. Nguyen, S. Su, T. L. Windus, M. Dupuis, J. A. Montgomery Jr., General atomic and molecular electronic structure system. *J. Comput. Chem.* **14**, 1347–1363 (1993).
51. S. Sakai, J. Soeda, R. Häusermann, H. Matsui, C. Mitsui, T. Okamoto, M. Ito, K. Hirose, T. Sekiguchi, T. Abe, M. Uno, J. Takeya, All solution-processed organic single-crystal transistors with high mobility and low-voltage operation. *Org. Electron.* **22**, 1–4 (2015).
52. J. Wang, R. M. Wolf, J. W. Caldwell, P. A. Kollman, D. A. Case, Development and testing of a general amber force field. *J. Comput. Chem.* **25**, 1157–1174 (2004).
53. C. I. Bayly, P. Cieplak, W. Cornell, P. A. Kollman, A well-behaved electrostatic potential based method using charge restraints for deriving atomic charges: the RESP model. *J. Phys. Chem.* **97**, 10269–10280 (1993).
54. H. J. C. Berendsen, J. P. M. Postma, W. F. van Gunsteren, A. DiNola, J. R. Haak, Molecular dynamics with coupling to an external bath. *J. Chem. Phys.* **81**, 3684–3690 (1984).
55. S. Nosé, A molecular dynamics method for simulations in the canonical ensemble. *Mol. Phys.* **52**, 255–268 (1984).
56. S. Nosé, A unified formulation of the constant temperature molecular dynamics methods. *J. Chem. Phys.* **81**, 511–519 (1984).
57. W. G. Hoover, Canonical dynamics: Equilibrium phase-space distributions. *Phys. Rev. A* **31**, 1695–1697 (1985).
58. M. Parrinello, A. Rahman, Polymorphic transitions in single crystals: A new molecular dynamics method. *J. Appl. Phys.* **52**, 7182–7190 (1981).
59. B. Hess, H. Bekker, H. J. C. Berendsen, J. G. E. M. Fraaije, LINCS: A linear constraint solver for molecular simulations. *J. Comput. Chem.* **18**, 1463–1472 (1997).
60. T. Darden, D. York, L. Pedersen, Particle mesh Ewald: An $N\cdot\log(N)$ method for Ewald sums in large systems. *J. Chem. Phys.* **98**, 10089–10092 (1993).
61. H. Horinouchi, H. Sakai, Y. Araki, T. Sakanoue, T. Takenobu, T. Wada, N. V. Tkachenko, T. Hasobe, Controllable electronic structures and photoinduced processes of bay-linked perylenediimide dimers and a ferrocene-linked triad. *Chem. Eur. J.* **22**, 9631–9641 (2016).
62. J. Mizuguchi, Phase change of N, N′-Bis (2-phenylethyl)perylene-3, 4:9, 10-bis (dicarboximide) for information storage applications. *Mol. Cryst. Liq. Cryst.* **322**, 291–298 (1998).
63. T. Uemura, C. Rolin, T.-H. Ke, P. Fesenko, J. Genoe, P. Heremans, J. Takeya, On the extraction of charge carrier mobility in high-mobility organic transistors. *Adv. Mater.* **28**, 151–155 (2016).
64. M.-M. Ling, P. Erk, M. Gomez, M. Koenemann, J. Locklin, Z. Bao, Air-stable n-channel organic semiconductors based on perylene diimide derivatives without strong electron withdrawing groups. *Adv. Mater.* **19**, 1123–1127 (2007).
65. B. A. Jones, A. Facchetti, M. R. Wasielewski, T. J. Marks, Effects of arylene diimide thin film growth conditions on n-channel OFET performance. *Adv. Funct. Mater.* **18**, 1329–1339 (2008).

Acknowledgments: We are grateful to H. Sato and A. Yamano at Rigaku Corporation for helpful single-crystal x-ray structure analyses. We also thank AGC Inc. for supplying AL-X601. The computations reported in this paper were performed at the Research Center for Computational Science, Okazaki, Japan. **Funding:** This work was supported by the JST-PRESTO program "Scientific Innovation for Energy Harvesting Technology" (number JPMJPR17R2) and by KAKENHI. T.O. and H.I. thank JSPS for Grants-in-Aid for Scientific Research, B (numbers 17H03104 and 18H01856). G.W. thanks JSPS for Grant-in-Aid for Scientific Research on Innovative Areas (number 19H05718). **Author contributions:** T.O. conceived and designed the work with significant input from J.T., while S.K., E.F., T.A., M.Y., Y.T., H.S., and T.W. synthesized the compounds. S.K. and M.Y. performed the single-crystal analyses, evaluated the electrochemical and physicochemical properties, conducted device experiments, and analyzed the data. S.K. and S.W. carried out the Hall effect measurements and analyzed the data. H.I. calculated the transfer integrals and effective masses. G.W. performed the MD simulations. N.N. calculated the intermolecular interaction energy values. T.O. and S.K. wrote the manuscript. T.O. and J.T. supervised the work. All authors discussed the results and reviewed the manuscript. **Competing interests:** The authors declare that they have no competing interests. **Data and materials availability:** Crystallographic data have been deposited in the CCDC as a supplementary publication under accession numbers CCDC-1938483 (PhC$_2$–BQQDI, 296 K), CCDC-1938480 (PhC$_2$–BQQDI, 373 K), CCDC-1938481 (C$_8$–BQQDI, 300 K), CCDC-1938482 (C$_8$–PDI, 298 K), and CCDC-1938639 (PDI–FCN$_2$, 298 K). These data can be obtained free of charge at https://nam12.safelinks.protection.outlook.com/?url=www.ccdc.cam.ac.uk%2Fdata_request%2Fcif&amp;data=01%7C01%7Cteaves%40aaas.org%7Cfeb8c76ddc0342356efc08d7a9875ea1%7C2eebd8ff9ed140f0a15638e5dfb3bc56%7C0&amp;sdata=j%2FuXjpca3dhy4mSyGNqG6EneBSKDEvr%2BmDaN6uBVFB8%3D&amp;reserved=0. Additional data related to this paper may be requested from the authors.

Submitted 8 August 2019
Accepted 7 February 2020
Published 1 May 2020
10.1126/sciadv.aaz0632

Citation: T. Okamoto, S. Kumagai, E. Fukuzaki, H. Ishii, G. Watanabe, N. Niitsu, T. Annaka, M. Yamagishi, Y. Tani, H. Sugiura, T. Watanabe, S. Watanabe, J. Takeya, Robust, high-performance n-type organic semiconductors. *Sci. Adv.* **6**, eaaz0632 (2020).